FACULTY OF SCIENCE
UNIVERSITY OF COPENHAGEN

Master's Thesis, Nanoscience

Jens Rix Nikolajsen

Thermoelectrically Driven Current Loops

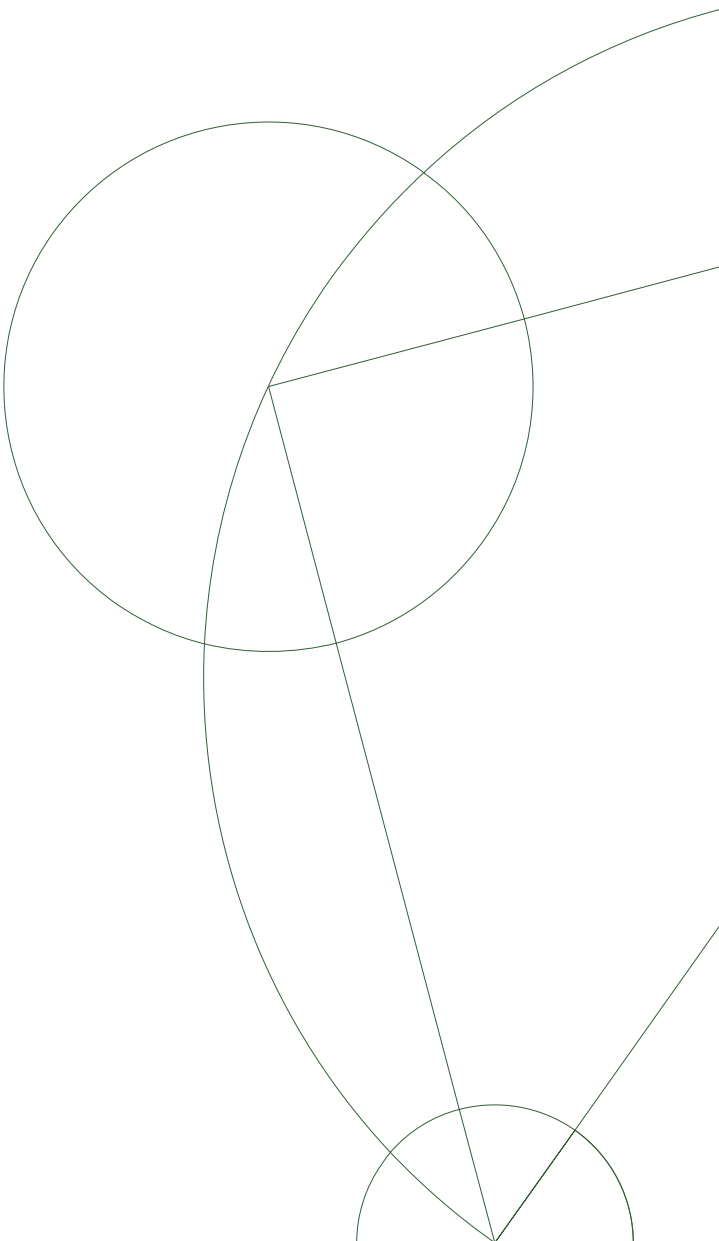

Supervisor: Prof. Per Hedegård

August 13, 2015

Abstract

The Seebeck effect was discovered almost 200 years ago, but in the search of effective thermoelectric power generators, the research field is still of interest. In Seebeck measurement, it is usually assumed that the electric current densities vanish as a reason of the canceled electric net current. In this thesis, we will argue that this assumption is wrong for inhomogeneous setups, in which the gradient of the Seebeck coefficient is not parallel to the temperature gradient, $\nabla S \times \nabla T \neq 0$. We will develop a finite element method procedure to calculate these current densities and present the resulting closed current loops. Based on this discovery in macroscopic systems, we will turn to electron transport through single molecules. Using Hückel theory and the transfer matrix formalism, we set up a calculation procedure for local bond currents in arbitrary molecules. As hypothesized, we find the existence of aromatic ring currents and we build some intuition on how to predict these currents.

Acknowledgements

First of all, I would like to thank my supervisor Professor Per Hedegård for good discussions, and for fighting my at times pessimistic viewpoints. Also thanks to our Chinese collaborators for the great experimental results.

Thanks to Anine Borger, Christoffer Florentsen and Jes Frederiksen for giving me feedback on the thesis and to Martin Larsen for good discussions. Also many thanks to the lunch club for good company.

Finally, thanks to my fiancée Anne for care and patience during the project.

Contents

Chapter 1

Introduction

In 1820, H. C. Ørsted did his famous discovery that an electric current induces a magnetic field. This is a well known moment in the scientific history and it was the beginning of electromagnetism as we know it today. Only one year later, a less known but very similar experiment was done by the Estonian-German physicist Thomas Johann Seebeck. He formed a loop consisting of two different materials, placed a compass magnet in the middle of the loop and heated it at a material junctions as sketched in figure 1.1. Just as Ørsted, Seebeck observed a deflection of the compass needle. Since it was in the very early days of electromagnetism and before Ohm's law was stated, Seebeck wrongly concluded that his observation was due to a thermomagnetic effect. The explanation was later corrected by Ørsted in the 1820's: The applied temperature difference drives an electric current, which induces the observed magnetic.

The experiment by Seebeck indicates the fundamental concept of the thermoelectric effects, i.e. heat transport and electric current are coupled. In addition to Ørsted's and Seebeck's observations, both temperature and electrical potential differences can drive a heat current.

Thermoelectrics (TEs) make it possible to convert waste heat into electrical energy and to transfer heat using electrical energy. These devices are known as TE generators and TE coolers respectively. TEs were originally expected to replace refrigerators and

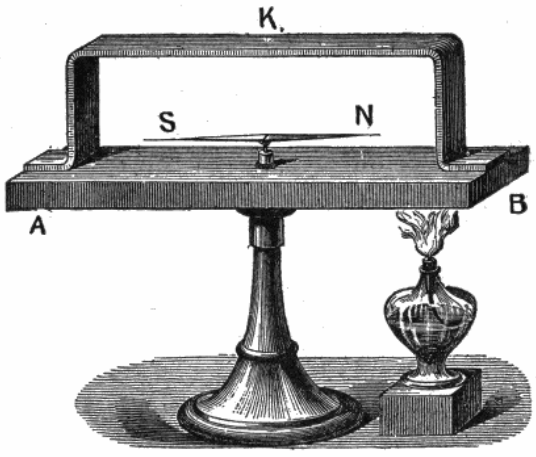

FIGURE 1.1: Illustration of the original experiment done by Seebeck.

to harvest waste heat from e.g. combustion engines. But due to low efficiency, those expectations and the interest in the field decreased. However, with the possibility to manipulate processes on the nanometer scale in the late 20th century, the interest increased once again. And here we are in a hot scientific field both to engineers and nanoscientists.

In this thesis, we will present the discovery of a misassumption in the literature on thermoelectricity. Under certain experimental conditions, electric current densities are expected to vanish, but we will show that loop currents can exist. These currents are the main topic of the thesis.

We will start from macroscopic setups and move to smaller length scales chapter by chapter. In this introduction, important concepts, formalism, and mathematical techniques are presented within the classical field description. These are used to model an experiment in chapter 2. In the process of modeling, the misassumption in the literature was detected, which led to an unsolved problem. In chapter 3 the problem is stated, a solution is found and the resulting loop currents are presented.

In the second part of the thesis, the existence of current loops in molecules is investigated using the tools of quantum mechanics. In chapter 4, thermopower in single molecules is introduced. The mathematical tools to calculate loop currents are developed in chapter 5, and the interesting results are presented.

1.1 Transport Equations

In this section, we will introduce the fundamental transport equations which will be the starting point for most calculations in the first three chapters.

Temperature is a diffuse quantity in molecules due to the small number of atoms. For macroscopic systems on the other hand, temperature is related to the local average of atom motion and due to the large number of atoms, it is reasonable to talk about a locally defined temperature. In the first three chapters we will treat macroscopic problems, and both temperature and electrical potentials are considered as well defined fields.

Variations in these fields can drive different currents. Consider for example a material subject to an electric field. Charges within the material will flow along the field lines and consequently the field drives an electric current. Since the charges are particles that can carry heat, the electric field can also drive a heat current. Similarly, a temperature gradient leads to diffusion of charges particles and therefore drives an electric current. If the applied fields are sufficiently small, the current responses are linear and can be stated in the general form:

$$\boldsymbol{J}_q = L_{qq}\nabla T + L_{qe}\nabla V \tag{1.1}$$
$$\boldsymbol{J}_e = L_{eq}\nabla T + L_{ee}\nabla V \ , \tag{1.2}$$

where $\boldsymbol{J}_q$ and $\boldsymbol{J}_e$ are the heat and electrical current density vectors of units $\frac{\mathrm{W}}{\mathrm{m}^2}$ and $\frac{\mathrm{A}}{\mathrm{m}^2}$, respectively. These equations can be shown e.g. in the free electron model by expanding the Fermi distribution function to linear order in the applied fields [1]. The general L coefficients were described experimentally during the 19th century. The direct electric response to an electric field follows from Ohm's law, $\boldsymbol{J}_e = -\sigma\nabla V$, where σ is

the electrical conductivity. The heat current driven by a temperature gradient has a contribution from both ordinary heat conduction described by Fourier's law ($-\kappa\nabla T$) and a contribution from the current of charged particles [2]:

$$\boldsymbol{J}_q = -\kappa\left(1 + \frac{\sigma S^2 T}{\kappa}\right)\nabla T = -\kappa'\nabla T \ , \tag{1.3}$$

where S is the Seebeck coefficient while κ is the thermal conductivity in the case of zero particle current. The reason for the this form of κ' will become clear when deriving Fourier's law under zero particle current conditions in section 1.2.1. The last term in the parenthesis is known as the figure of merit $ZT = \frac{\sigma S^2 T}{\kappa}$. For metals and ordinary semiconductors, this dimensionless quantity is very small [1, 3] and for all materials used in this thesis it is on the order $ZT \sim 0.001$. We will therefore use $\kappa' \approx \kappa$ except when connecting the thermoelectric generator efficiency to the figure of merit in sec. 1.4. The cross effects in eqs. (1.1) and (1.2) were described by Seebeck and Peltier, and we will go through their experiments in the following section. The final transport equations can be stated as:

$$\boldsymbol{J}_q = -\kappa'\nabla T - TS\sigma\nabla V \tag{1.4}$$

$$\boldsymbol{J}_e = -S\sigma\nabla T - \sigma\nabla V \ , \tag{1.5}$$

With this sign convention of S, a material dominated by positive charge carriers will have a positive Seebeck coefficient and vice versa. The Seebeck coefficients are temperature dependent, but we will only consider small temperature changes and therefore neglect this dependence. All variables in eqs. (1.4) and (1.5) depend on position, which is left out to keep the notation simple. To calculate the current densities at a specific position from these equations alone, the temperature and electrical potential fields have to be known. However, in an experimental setup, the temperature and potential are only known at the boundaries, and the equations need to be solved as boundary value problems. We will return to this several times during the thesis.

From the final transport equations (1.4) and (1.5) we see that the cross-effect coefficients $L_{qe} = -TS\sigma$ and $L_{eq} = -S\sigma$ are dependent variables, $L_{qe} = TL_{eq}$. This symmetry is a general property in coupled transport systems as described theoretically by Onsager around 80 years after the experimental discovery [4]. Onsager's reciprocal relations are valid in time reversal symmetric systems. In this thesis we do not consider any applied magnetic fields, and the relation $L_{qe} = TL_{eq}$ is therefore valid.

1.2 Thermoelectric Effects

With the transport equations (1.4) and (1.5) as a starting point, we will in this section describe the most important thermoelectric effects. Using a simple argument, we show that the assumption $\boldsymbol{J}_e = 0$ in Seebeck measurement is not generally true.

The Seebeck and Peltier effects provide the basic concepts of thermoelectric generators and coolers respectively. In this sense the effects are each others inverse. But despite the great difference in the physical concepts, they are just results of the transport equations

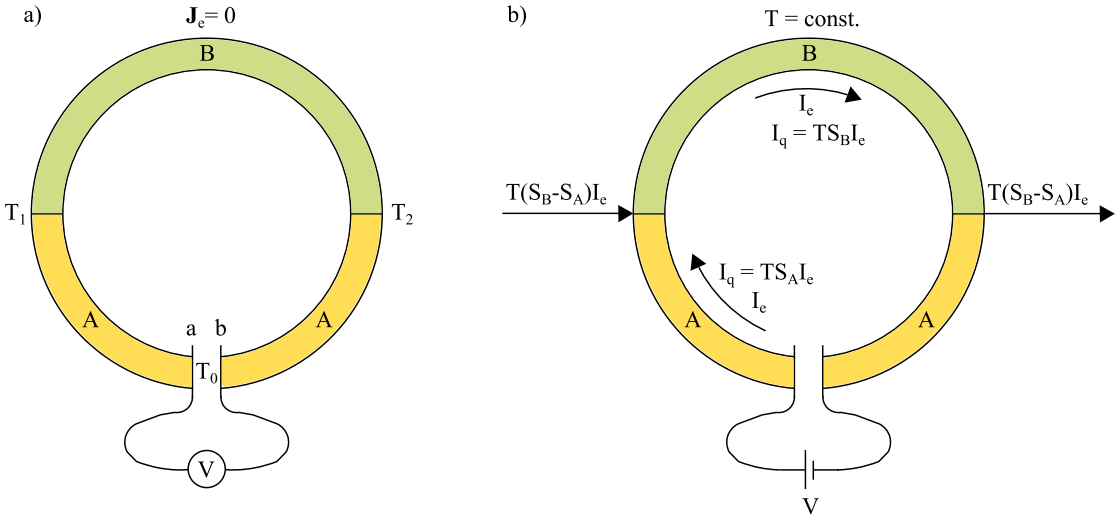

FIGURE 1.2: Schematics showing two differently connected bimaterial rings. a) Thermocouple: a temperature difference is applied and the resulting electrical potential is measured. b) The Peltier effect: the temperature is kept constant and an electrical current is driven by an applied voltage difference. Consequently heat must be supplied at one material junction and extracted at the other.

subject to different boundary conditions. In this section we will describe the effects in closed loops composed of two materials. This is a theoretically clean starting point which illustrates that the Seebeck coefficient is a relative quantity.

1.2.1 The Seebeck Effect

In the original Seebeck experiment shown in fig. 1.1, we see the coupling between heat and charge transport. The applied temperature difference at the material junctions ensures that the temperature drop is the same in both materials in the loop. As a response to this temperature gradient, electric current of different intensities are generated in each material A and B depending on the material constants in eqs. (1.4) and (1.5). If $\sigma_A S_A = \sigma_B S_B$, the generated electric current in material A will cancel that from material B, and we would not observe a deflection of the magnetic needle.

In order to quantitate the Seebeck coefficients, a voltmeter is added to the loop as shown in fig. 1.2a. This particular setup is known as a thermocouple. The diffusing charges will then accumulate close to the voltmeter and alter the electrical potential. The resulting electric field forces the charges in the opposite direction, and a steady-state situation is eventually reached where $I_e = 0$. By I_e we mean the total current in contrast to $\boldsymbol{J}_e$ which is the current density. In textbooks it is assumed that the cancellation of the net current in general causes the electrical current densities to vanish, $I = 0 \Rightarrow \boldsymbol{J_e} = 0$ [1, 3]. As we will argue shortly, this is not necessarily true for anisotropic materials or inhomogeneous systems of higher dimensions than 1. Accepting the assumption $\boldsymbol{J_e} = 0$ for now, eq. (1.5) reduces to:

$$\nabla V = -S\nabla T \ . \tag{1.6}$$

TABLE 1.1: Material constants to be used throughout the thesis. Thermal and electrical conductivities are obtained from Kaye & Laby [5]. The Seebeck are measured against Pt [6]. Information on BDT crystal is to be used in the following chapter. (*) The thermal conductivity for BDT crystals is unknown, but films of organic compounds take values 0.2-0.5 [7]. (**) Value obtained in chapter 2.

	κ $[\frac{\mathrm{W}}{\mathrm{m\cdot K}}]$	σ $[\frac{10^6}{\Omega \mathrm{m}}]$	S $[\frac{\mu \mathrm{V}}{\mathrm{K}}]$
Gold	319	48.8	6.5
Platinum	72	10.2	0
Aluminum	236	41.3	3.5
BDT crystal	0.35*	unknown	413**

The Seebeck coefficient is thus the proportionality factor between the generated electric field and the applied temperature difference. This is also known as the thermopower. The heat current can be expressed by inserting eq. (1.6) into eq. (1.4) so that $\boldsymbol{J}_q = -\kappa' \nabla T - TS\sigma \nabla V = -\kappa \nabla T$. Since the transport of charged particles is zero in this case, the only contribution to the heat current is the ordinary Fourier heat conduction. This is the reason for the extra term in the heat current in eq. (1.3). The potential difference measured by the voltmeter in fig. 1.2a can be related to the temperature difference by integrating along the wire $\Delta V = \int_a^b \nabla V \cdot d\boldsymbol{s} = V_b - V_a$:

$$\Delta V = -\int_{T_0}^{T_1} dT S_A - \int_{T_1}^{T_2} dT S_B - \int_{T_2}^{T_0} dT S_A \tag{1.7}$$

$$= (S_A - S_B)\Delta T \ , \tag{1.8}$$

where $\Delta T = T_2 - T_1$. In the last step we have neglected the temperature dependence of the Seebeck coefficients, which is reasonable for small temperature differences. We now have a relation between the temperature difference and the build up potential difference. From this textbook example, two important facts should be noted. The first fact is that for know T_1, ΔV and the relative Seebeck coefficient between the two materals A and B, the temperature T_2 can be calculated. This fact makes the thermocouple a useful tool for measuring the temperatures. The second fact is that Seebeck coefficients are measured relative to each other. This is important when thermoelectric components are considered in an open circuit; the temperature drop in the component is also present in the connecting cables and measuring equipment, and the Seebeck coefficient is therefore measured relative to the rest of the circuit. In table 1.1, Seebeck coefficients relative to Platinum are listed together with thermal and electrical conductivities for materials of interest in this thesis.

We will now return to the assumption that the current density vanishes $\boldsymbol{J}_e = 0$ in the Seebeck measurement. Consider a two-dimensional component consisting of two isotropic materials A and B as shown in fig. 1.3. The temperature on the left and right boundaries are T_L and T_R, respectively. For an arbitrary path connecting the left and right contacts as sketched in the figure, the sum of all current densities along the path is:

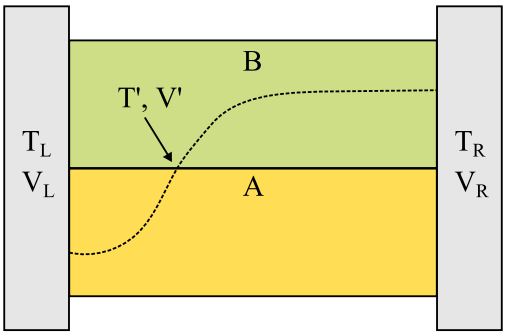

FIGURE 1.3: Schematics of a 2D inhomogeneous sample connected by the two contacts in grey. The dashed line is an arbitrary path which crosses the material border at a point with temperature and potential T' and V'.

$$\int \boldsymbol{J}_e \cdot d\boldsymbol{s} = -S_A\sigma_A(T' - T_L) - S_B\sigma_B(T_R - T') - \sigma_A(V' - V_L) - \sigma_B(V_R - V') \tag{1.9}$$

$$= S_A\sigma_A T_L - S_B\sigma_B T_R + \sigma_A V_L - \sigma_B V_R - (S_A\sigma_A - S_B\sigma_B)\,T' - (\sigma_A - \sigma_B)\,V' \,. \tag{1.10}$$

In the homogeneous case where $S_A = S_B$ and $\sigma_A = \sigma_B$, the prime terms drop out and we are left with $\int \boldsymbol{J}_e \cdot d\boldsymbol{s} = -S_A\sigma_A\Delta T - \sigma_A\Delta V$, independent of the choice of integration path. For a particular temperature difference, we can therefore choose a potential difference which cancel the integral. Since the current is divergenceless (from the steady state continuity equation, $\nabla \cdot \boldsymbol{J}_e = 0$) and the integration path can be chosen arbitrarily, this argument confirms that the current densities vanish in homogeneous samples. Equation (1.6) is therefore verified in the homogeneous case.

If the materials A and B are different, we are left with the prime terms in eq. (1.10) and the problem is more complicated. For the particular path shown in fig. 1.3, there exists a potential difference which cancels the electric current contribution. The value can be obtained from a boundary value problem, but it is not important here. If we then alter the path so that the material boundary is crossed at another point with $T'' \neq T'$ and $V'' \neq V'$, this new path might contribute to an electric current. There is therefore no unique potential difference that cancels all current densities, and consequently the reduction of the transport equation to $\nabla V = -S\nabla T$ is not always valid for inhomogeneous setups of 2 or 3 dimensions. We will return to this problem in chapter 3.

A similar argument holds for an anisotropic sample. If the current from one path is canceled by an applied potential difference, another path with a different starting point might contribute to the current. We will not focus on anisotropy in this thesis.

1.2.2 The Peltier Effect

The Peltier effect is another thermoelectric effect that follows from the transport equations. Consider the bimaterial ring connected as shown in fig. 1.2b. A potential difference is applied to the loop and we require that the temperature T is constant in the entire sample. Since the temperature gradient vanishes, the transport equations (1.4) and (1.5) reduce to $\boldsymbol{J}_q = -TS\sigma\nabla V$ and $\boldsymbol{J}_e = -\sigma\nabla V$. Eliminating the electric field, we see that the currents are connected in the following way:

$$\boldsymbol{J}_q = TS\boldsymbol{J}_e \ . \tag{1.11}$$

Since the electric current $I_e = \int \boldsymbol{J}_e \cdot d\boldsymbol{a}$ is the same everywhere along the loop, the different heat currents $I_{q,A} = TS_A I_e$ and $I_{q,B} = TS_B I_e$ are flowing in material A and B, respectively. Notice that I_q has units W. For the energy to be conserved, we therefore have to add the thermal energy $\dot{Q} = I_{q,B} - I_{q,A}$ in the left junction and remove it from the right junction:

$$\dot{Q} = T\left(S_B - S_A\right) I_e \ . \tag{1.12}$$

The Peltier effect was observed by the French physicist Jean Charles Athanase Peltier in the 1830s. This was before the knowledge of the transport equations of the form discussed, and for historical reasons the notation $\boldsymbol{J}_q = \Pi \boldsymbol{J}_e$ is sometimes used, where Π is the Peltier coefficient. The first Thomson relation $\Pi = TS$ was stated twenty years and as mentioned, the coupling was proved theoretically around 80 years later.

In the Peltier effect, electrical energy is consumed with the result that heat is transferred from one material junction to the other. It therefore has the property of cooling and provides the basic idea of thermoelectric coolers.

As mentioned, the Seebeck and Peltier effects are basically just results of the transport equations solved with different boundary conditions. Suppose e.g. that we start out with the Peltier effect in fig. 1.2b and suddenly change the boundary conditions, so that the loop is thermally insulated at the material junctions. The loop will then heat up at one junction and cool down at the other depending on the relation between the Seebeck coefficients. The build up temperature difference will lead to diffusion of charge carriers and a steady-state situation is eventually reached, where the drift and diffusion of charges cancel each other out. Thus, the change in boundary conditions lead us from Peltier effect in fig. 1.2b to the Seebeck effect in fig. 1.2a.

1.2.3 Other Thermoelectric Effects

Another thermoelectric effect is the Thomson effect in which the heat loss associated with the temperature dependence of the Seebeck coefficient is considered. From particle-number and energy conservation, the continuity equations lead to the generated heat in a small volume per unit time: $\frac{\partial q}{\partial t} = -\boldsymbol{J}_e \cdot \nabla V - \nabla \cdot \boldsymbol{J}_q$. By inserting the transport equations into this expression we get:

$$\frac{\partial q}{\partial t} = \frac{1}{\sigma}\boldsymbol{J}_e^2 - \mu_T \boldsymbol{J}_e \cdot \nabla T \ , \tag{1.13}$$

where the first term is the ordinary Joule heat and the second term is the so-called Thomson heat. The coefficient μ_T is related to the Seebeck coefficient through the second Thomson relation:

$$\mu_T = T\frac{\partial S}{\partial T} \ . \tag{1.14}$$

The situations considered in this thesis operate at relatively small temperature differences. The Seebeck coefficients are therefore considered independent of temperature and the Thomson effect is neglected.

Several other effects appear when a magnetic fields is applied in addition to either a temperature gradient or a potential gradient. One example is the Nernst effect, which has great similarities to the Hall effect. In the Nernst effect, a temperature gradient is applied to a piece of conducting material so that the charged carriers flow from hot to cold. Perpendicular to this flow, a magnetic field is applied and the Lorentz force acts on the charges perpendicular to both the temperature gradient and the magnetic field. Consequently, a potential difference builds up due to the accumulation of charges on the transverse edges:

$$\nabla V = A_{\mathrm{N}} \boldsymbol{B} \times \nabla T \ , \tag{1.15}$$

where A_{N} is the Nernst coefficient. Just like the Seebeck effect, the Nernst effect is another example of a thermoelectric generator, i.e. a setup in which thermal energy is converted into electrical energy.

1.3 Thermoelectric Components in Open Circuits

Until now we have explained the thermoelectric effects and provided the governing local transport equations. In this section, we will describe the Seebeck effect in a circuit. Despite the simplicity of the consideration, the derived expressions will be used throughout the thesis.

We will now return to the Seebeck effect and study parallel and serial connections of thermoelectric components characterized by an electrical resistance R, a thermal resistance R_q and a Seebeck coefficient S. This is again a one-dimensional consideration which requires the temperature and electrical potential gradients to point along the materials. The component picture is still used in recent articles [8], and we will use it in chapter 2 to describe a real experimental setup.

The transport equations (1.4) and (1.5) describe the local current densities. For a single piece of material with cross section area A, the equations can be rewritten as:

$$I_q = \frac{1}{R_q}\Delta T + \frac{TS}{R}\Delta V \tag{1.16}$$

$$I_e = \frac{S}{R}\Delta T + \frac{1}{R}\Delta V \ , \tag{1.17}$$

after multiplying with A and integrating along the length. The signs are chosen so that the currents are in the direction from the hot (h) to the cold (c) contact and the differences are $\Delta V = V_h - V_c$ and $\Delta T = T_h - T_c$. In an open circuit, the temperature drop across the system of interest is also present in the connecting circuit. The Seebeck coefficient of the system is therefore relative to an unknown S_{circuit}. In order to measure Seebeck coefficients, the particular experimental setup therefore needs to be calibrated

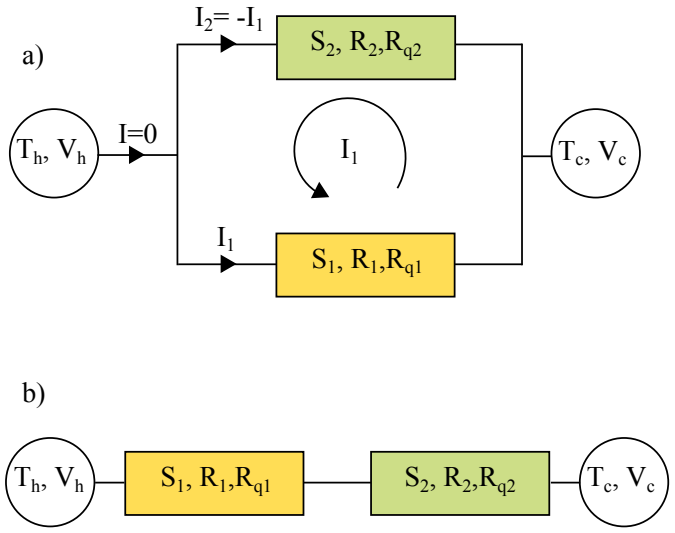

FIGURE 1.4: Thermoelectric elements in parallel (a) and series (b). R, R_q and S denote the electrical resistance, thermal resistance and Seebeck coefficient of each element, respectively.

with a known material prior to the measurement. We will return to this fact in chapter 2.

1.3.1 Parallel Setup

In this section we will look at the Seebeck coefficient of components in parallel. We will see the existence of an internal current loop even though the net current is zero. This is an important result which we will return to in the discussion of both inhomogeneous systems in 3D and molecules.

Consider first the simple parallel setup shown in fig. 1.4a. The electric current through each component is given by eq. (1.17) and the total electric current is therefore

$$I = I_1 + I_2 = \left(\frac{1}{R_1} + \frac{1}{R_2}\right)\Delta V + \left(\frac{S_1}{R_1} + \frac{S_2}{R_2}\right)\Delta T \ . \tag{1.18}$$

If the potential difference is tuned so that the net current cancels, $I = 0$, we get the effective Seebeck coefficient for the parallel connected components $S = -\Delta V/\Delta T$:

$$S_{\text{parallel}} = \frac{R_2 S_1 + R_1 S_2}{R_1 + R_2} \ . \tag{1.19}$$

In the case where $R_1 \ll R_2$, we see that the effective Seebeck coefficient becomes $S_{\text{parallel}} \to S_1$. Similarly if the materials are identical so that $S_1 = S_2 = S$ and $R_1 = R_2 = R$, the measured value reduces to $S_{\text{parallel}} \to S$. We now insert the potential difference $\Delta V = -S_{\text{parallel}}\Delta T$ into the expression for the current in the loop:

$$I_1 = \frac{1}{R_1}\Delta V + \frac{S_1}{R_1}\Delta T \tag{1.20}$$

$$= \frac{1}{R_1}\left(-S_{\text{parallel}} + S_1\right)\Delta T \tag{1.21}$$

$$= \frac{S_1 - S_2}{R_1 + R_2}\Delta T \ . \tag{1.22}$$

This result shows that even though the net current through a parallel setup is zero, there might be an internal loop current. For the loop current to be non-zero, the components need to have different Seebeck coefficients. Furthermore both components should conduct electrical current so that the denominator is not too large.

This observation of an internal current loop under the zero-net-current condition is a simple explanation for the existence of internal currents loop in inhomogeneous systems. Such currents will be calculated in chapter 3 and compared to eq. (1.22).

1.3.2 Serial Setup

We here turn to components connected in series. This consideration will be used to model an experimental setup in chapter 2.

Consider the two components in series as sketched in fig. 1.4b. Under the zero net current condition, the potential difference is $\Delta V = \Delta V_1 + \Delta V_2 = -(S_1\Delta T_1 + S_2\Delta T_2)$. The temperature difference is found from the Fourier law, $\Delta T = \Delta T_1 + \Delta T_2 = I_q(R_{q1} + R_{q1})$. Using these equations, the effective Seebeck coefficient of the serial setup can be expressed as

$$S_{\text{serial}} = \frac{S_1 R_{q1} + S_2 R_{q2}}{R_{q1} + R_{q2}} \ . \tag{1.23}$$

The factor in front of each Seebeck coefficient is an expression for the temperature drop across the particular component compared to the entire temperature drop. For example $\Delta T_1/\Delta T = R_{q1}/(R_{q1} + R_{q2})$. If $R_{q1} > R_{q2}$ the main temperature drop will be across component 1, and S_1 will dominate the effective Seebeck coefficient. We will return to eq. (1.23) in chapter 2, where it is used to model an experimental setup.

1.4 Figure of Merit

The thermoelectric generator efficiency of a material depends on the figure of merit, ZT. In this section we will derive an expression for the efficiency to see how it relates to ZT and how ZT relates to the material constants.

Consider a thermoelectric material characterized by κ, σ and S. The material is heated on one side and an electrical potential difference builds up to cancel the electric currents. If we connect an electrical load to the hot and cold sides, an electric current will run through the load due to the potential difference as sketched in fig. 1.5. We now want

to investigate how the material properties κ, σ and S affect the power efficiency defined as:

$$\eta = \frac{\text{Power output at load}}{\text{Power input at heat source}} , \tag{1.24}$$

where η takes values between 0 and 1. In order to calculate this quantity, we will use the circuit transport equations. The full thermal conductivity κ' in eq. (1.4) is important in this case, since we will look at materials with a high factor $\sigma S^2 T/\kappa$, and the heat current takes the form: $I_q = \frac{1}{R_q}\left(1 + \frac{R_q S^2 T}{R}\right)\Delta T + \frac{TS}{R}\Delta V$. For the electric current, eq. (1.17) is used. The power output at the load is $I_e \cdot (V_c - V_h) = -I_e \Delta V$, while the input power is the heat current inserted to the system. After some rewriting, the efficiency is:

$$\eta = -\frac{I_e \Delta V}{I_q} \tag{1.25}$$

$$= -\frac{\left(\frac{1}{R}\Delta V + \frac{S}{R}\Delta T\right)\Delta V}{\frac{TS}{R}\Delta V + \frac{1}{R_q}\left(1 + \frac{R_q S^2 T}{R}\right)\Delta T} \tag{1.26}$$

$$= -\Delta T \frac{\left(\frac{\Delta V}{\Delta T}\right)^2 + S\frac{\Delta V}{\Delta T}}{TS\frac{\Delta V}{\Delta T} + \frac{R}{R_q}\left(1 + \frac{R_q S^2 T}{R}\right)} \tag{1.27}$$

We have only applied the temperature difference, while the potential difference is a response of the system. The ratio between the potential and temperature difference can be expressed through the load resistance. The electrical current is $I_e = \frac{1}{R}\Delta V + \frac{S}{R}\Delta T = -\frac{\Delta V}{R_{\text{load}}}$, which can be rewritten as:

$$\frac{\Delta V}{\Delta T} = -\frac{S R_{\text{load}}}{R + R_{\text{load}}} . \tag{1.28}$$

The idea is now to tune the load resistance so that we achieve the maximum power efficiency. Inserting eq. (1.28) into (1.27) and maximizing with respect to R_{load}, we find that $R_{\text{load,op}} = R\sqrt{1 + ZT}$, where $ZT = \frac{R_q S^2 T}{R}$ is the so-called figure of merit. We will return to this shortly. Inserting the optimized load resistance into the expression for η, the maximum efficiency can be put on the form:

$$\eta = \frac{\Delta T}{T}\frac{\sqrt{1 + ZT} - 1}{\sqrt{1 + ZT} + 1} . \tag{1.29}$$

Consequently the efficiency of a thermoelectric generator only depends on the material constants through the introduced figure of merit, ZT. The efficiency is a monotonically growing function with ZT and scientists therefore search for materials with as high a ZT as possible. Canceling the cross section area and length, the unitless figure of merit is expressed as:

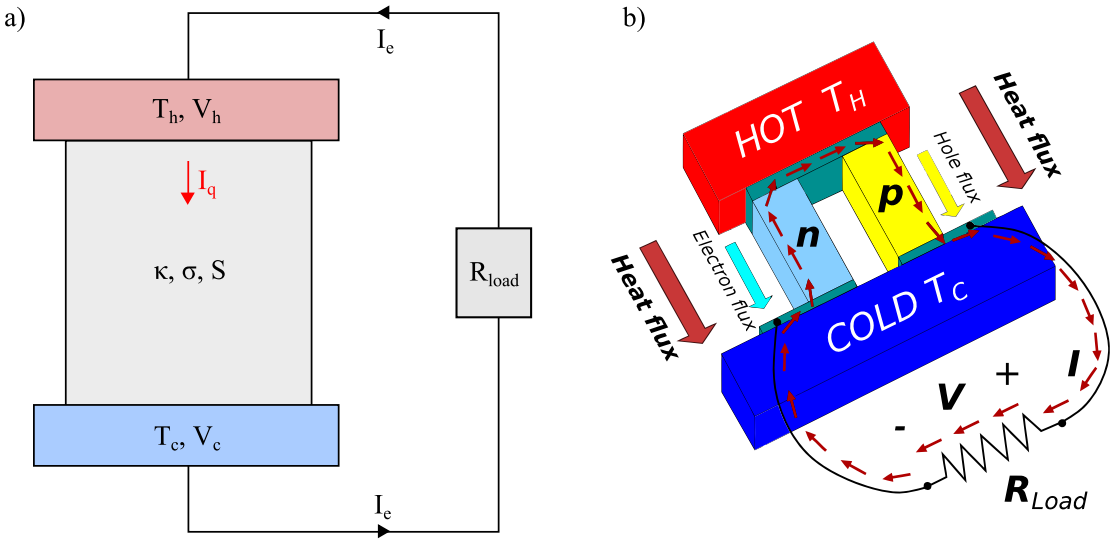

FIGURE 1.5: a) Schematic diagram of a thermoelectric generator. An applied temperature difference drives an electric current, from which energy is withdrawn in the load. b) A modern TEG that uses the combination of materials with positive and negative charge carriers [9].

$$ZT = \frac{\sigma S^2 T}{\kappa} \,. \tag{1.30}$$

One of the best figures of merit recently reported is $ZT = 2.62$ [10]. Using this particular ZT as an example, the resulting efficiency is $\eta = 0.31 \cdot \frac{\Delta T}{T}$. For a temperature difference of 10 K at room temperature, the Carnot efficiency yields $\frac{\Delta T}{T} = 3.4\%$. Consequently TE generators are still very inefficient for room temperature applications.

To increase the efficiency, thermoelectric generators are usually constructed as shown in fig. 1.5b [9]. In this clever setup, electrons and holes follow the temperature gradient in the negatively and positively doped semiconductors respectively. In this way, both materials contribute to an electric current in the same direction as shown with small red arrows.

To sum up, the efficiency of a thermoelectric generator is related to the material constants via the figure of merit in eq. (1.30). The higher the figure of merit, the more efficient is the TEG.

1.5 Differential Equations with Boundary Conditions

Until now we have encountered several differential equations and manipulated them both locally and with boundaries in 1D. In chapter 2, we will consider a specific three-dimensional experimental setup, and we therefore want to find solutions in a volume $\mathcal{V}$. In such a problem we know specific values or conditions on the boundaries to the volume, and it can therefore be solved as a boundary value problem.

We will deal with two kinds of boundaries in this thesis, namely the Dirichlet boundary conditions (bc) and the Neumann bc. When solving a differential equation of a scalar

field f, the Dirichlet bc requires that the value of f is known on the entire boundary. For the Neumann bc, the gradient of f perpendicular to the boundary is known on the entire boundary. Imposing either of these boundary conditions, any ordinary or partial differential equation has a unique solution in the interior volume $\mathcal{V}$ (for Neumann bc, this is true up to a constant). The same holds for mixed boundary conditions where Dirichlet bc are imposed over parts of the boundaries and Neumann bc on the rest.

As an example, let us consider the temperature Laplace equation, $\nabla T = 0$, which is known as the steady-state homogeneous heat equation. The uniqueness of the boundary value problem of the Laplace is easily demonstrated [11]. As a starting point, consider the divergence theorem:

$$\iiint_{\mathcal{V}} dV\,(\nabla \cdot \boldsymbol{A}) = \oiint_{S} dS(\boldsymbol{A} \cdot \hat{\boldsymbol{n}})\ , \tag{1.31}$$

where $\boldsymbol{A}(\boldsymbol{r})$ is an arbitrary well-behaved vector field. If we look at a vector field defined by $\boldsymbol{A} = f\nabla f$, where $f(\boldsymbol{r})$ is an arbitrary scalar field, the divergence theorem can be rewritten as:

$$\iiint_{\mathcal{V}} dV\,\left(f\nabla^2 f + \nabla f \cdot \nabla f\right) = \oiint_{S} dS\left(f\frac{\partial f}{\partial n}\right)\ , \tag{1.32}$$

where $\frac{\partial f}{\partial n} = \nabla f \cdot \hat{\boldsymbol{n}}$ is the gradient perpendicular to the surface. For the steady-state heat equation, $\nabla^2 T = 0$, we suppose that there are two solutions $T_1(\boldsymbol{r})$ and $T_2(\boldsymbol{r})$ inside a region with the same imposed boundary conditions. If we define the scalar field $f(\boldsymbol{r}) = T_2(\boldsymbol{r}) - T_1(\boldsymbol{r})$ and insert f into equation (1.32), we get:

$$\iiint_{\mathcal{V}} dV|\nabla f|^2 = 0\ . \tag{1.33}$$

Here it is used that both solutions T_1 and T_2 are solutions to the Laplace equation so that $\nabla^2 f = 0$. The right side of (1.32) vanish for Dirichlet boundaries since $T_1(\boldsymbol{r}_{\text{edge}}) = T_2(\boldsymbol{r}_{\text{edge}}) \ \Rightarrow \ f = 0$. The same argument holds for Neumann boundaries $\frac{\partial f}{\partial n} = 0$. Consequently the right-hand-side also vanishes for mixed boundaries.

For eq. (1.33) to be true, the scalar field f has to be constant everywhere in the interior volume $\mathcal{V}$. In the case of Dirichlet bc, $f = T_1 - T_2 = 0$ on the boundary and therefore on the entire volume $\mathcal{V}$. Thus, $T_1(\boldsymbol{r}) = T_2(\boldsymbol{r})$ is a unique solution. For pure Neumann conditions, f can take any constant value, and the solution is only unique up to a constant $T_1(\boldsymbol{r}) = T_2(\boldsymbol{r}) + c$. In this thesis we will only solve mixed boundary value problems, and the solutions are therefore always unique.

In the following we will mostly deal with rotationally symmetric systems and therefore use cylindrical coordinates. For simple cylinder Dirichlet boundary problems, the Laplace equation $\frac{1}{r}\frac{\partial}{\partial r}\left(r\frac{\partial f}{\partial r}\right) + \frac{\partial^2 f}{\partial z^2} = 0$ can be solve analytically using separation of variables $f(r,z) = R(r)Z(z)$ [11]. The radial part is solved by Bessel functions of the first kind, while the Z-part is solved by exponential functions. The general solution is a linear combination of these with coefficients determined by the boundary conditions.

Since we will be dealing with more complicated geometries, separation of variables is not an option. The differential equations are instead solved numerically using the finite element method (FEM) in Mathematica 10. In FEM, the region in which the partial differential equation is to be solved is divided into a mesh of finite elements, i.e. a grid of smaller domains. Finding the solution is then a technical matter of solving element equations for each element and combining these into a global solution, which is done by the computer. The design of the mesh can influence the result of a FEM calculation. For the calculations done in this thesis, the mesh is defined to be fine masked in regions where the scalar field gradients of interest are large.

With this introduction to solving boundary value problems, we will now demonstrate how to obtain the temperature and electrical potential fields in a homogeneous setup.

1.5.1 Thermopower in Homogeneous Systems

In this section, we will see how the temperature and potential maps are calculated in the interior of a setup with known boundaries.

For Seebeck measurements of homogeneous setups, i.e. setups where the material constants do not depend on position, the temperature and potential fields can easily be calculated using the theory described in the section 1.2.1. The electric current density is canceled by the applied electrical potential difference and eq. 1.5 reduces to $\nabla V = -S\nabla T$. The problem is therefore reduced to calculating the temperature field from which the potential field easily follows.

The temperature field can be found from the heat equation. From conservation of energy follows the continuity equation, $\frac{\partial u}{\partial t} + \nabla \cdot \boldsymbol{J}_q = 0$, where u is the local energy density. Inserting the expression for the heat current density $\boldsymbol{J}_q = -\kappa\nabla T$, the homogeneous steady-state heat equation is:

$$\nabla^2 T(\boldsymbol{r}) = 0 \tag{1.34}$$

To get the temperature and potential fields of a specific sample, the Laplace equation for the temperature is solved using the FEM as described in the previous section. If the electrical potential is known at any point $\boldsymbol{r}_0$ on the boundary with value V_0 (at which the temperature is T_0), the potential map can be found by doing a line integral from this point $V(\boldsymbol{r}) = V_0 + \int_{\boldsymbol{r}_0}^{\boldsymbol{r}} \nabla V \cdot d\boldsymbol{l}$:

$$V(\boldsymbol{r}) = V_0 + S\left(T_0 - T(\boldsymbol{r})\right) \ . \tag{1.35}$$

As an example, we consider a piece of gold shaped as a small cylinder on top of a larger cylinder with the cross section shown in fig. 1.6a. The bottom boundary of the piece is kept at 310 K and the top at 300 K. The rest of the surface is thermally insulated, which is insured using the Neumann bc. By solving the homogeneous steady-state heat equation, we get the temperature map shown in fig. 1.6b. Since the thermal resistance is largest in the small cylinder, this is where the main temperature drop takes place. Using eq. (1.35), the electrical potential is easily calculated and the result is shown in fig. 1.6c.

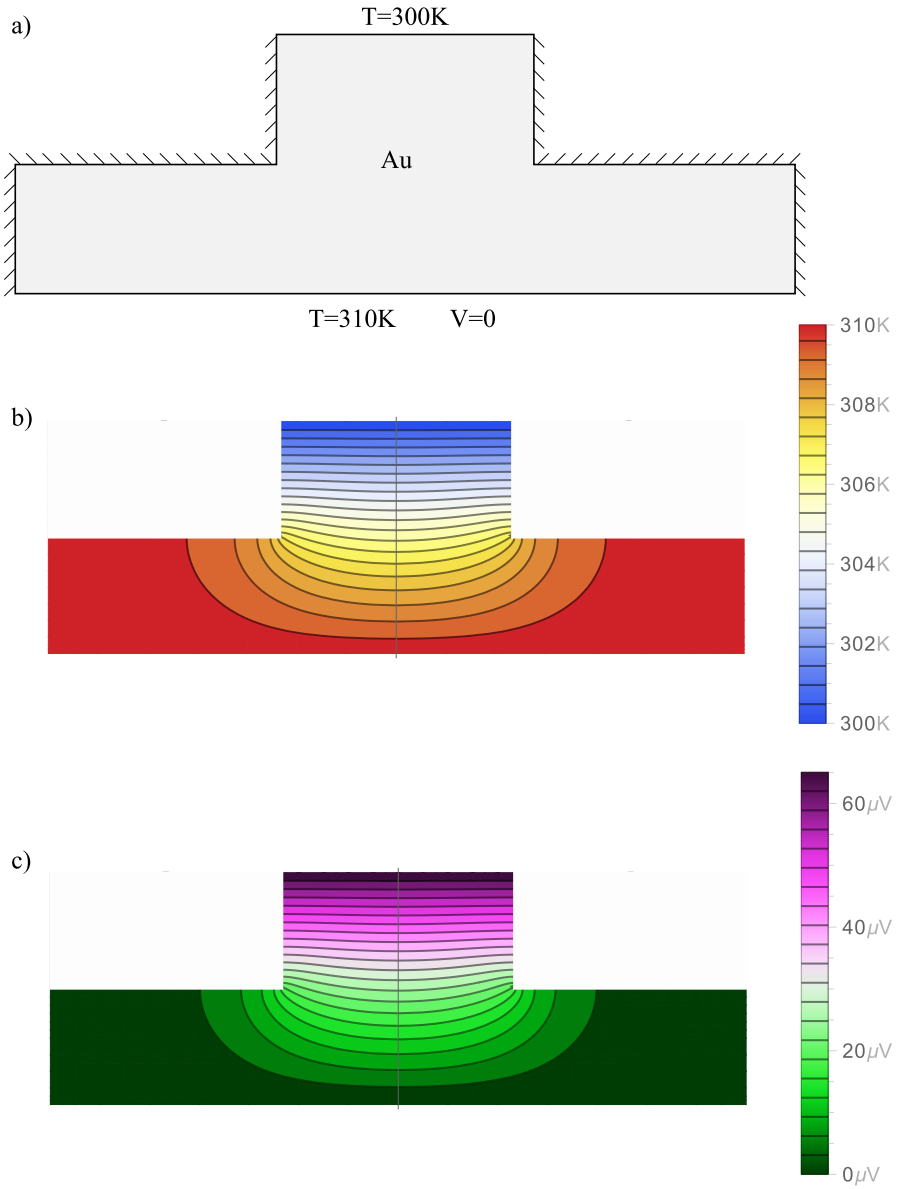

FIGURE 1.6: a) Cross-section of a cylinder-on-cylinder shaped piece of gold. The thin lines on the boundaries indicate thermally insulation, while the top and buttom take the shown Dirichlet conditions. b and c) Resulting temperature and electrical potential maps obtained from the FEM calculation.

The simplification of the transport equation to $\nabla V = -S\nabla T$ is not valid for all inhomogeneous systems, as indicated in section 1.2.1. We will discuss this more carefully in chapter 3 and show how the temperature and potential fields are calculated in such setups.

Chapter 2

Measurement on Length Dependent Thermopower

From macroscopic components in a circuit, we now turn to a smaller length scale. As mentioned in the introduction, the emergence of nanotechnology lead to an increased interest in the field of thermoelectrics. The reason for this is that molecular compounds can be manipulated so that the figure of merit is optimized. As an example, it has been demonstrated that going from bulk materials to thin-films of a few μm improves ZT [12]. In this chapter, we are going to investigate experimental results of organic thin-films on the nanometer scale.

When measuring the Seebeck coefficient of an organic thin-film, a conventional thermocouple setup would damage the sample. Instead the concepts of atomic force microscopy (AFM) and scanning tunneling microscopy (STM) have been used to form scanning thermal microscopes (SThM) and scanning thermopower microscopes (STPM). In its basic form, an STPM is a STM with attached thermocouples on the tip and under the sample. This was already used in 1995 to measure monolayers of guanine [13]. Since then the technique has been advanced to include thermocouples inside the tip [14]. The data in the following is obtained from a modified STM.

2.1 The Experiment

The initial task of this masters project was to analyze experimental results from a thermopower measurement done by collaborators at Chinese Academy of Science, Beijing. The organosulfur compound bis(dithienothiophene), BDT, was self-assembled into monolayers or layered structures at a desired thickness and placed in the experimental setup shown in figure 2.1a. Here a 30 nm thick layer of gold was placed on top of a macroscopic piece of silicon (thickness $\sim$ 800 μm) and connected to a platinum tip through the circuit as shown in the figure. The setup was heated from underneath the Si layer so that the heat would flow through the Si, Au, BDT sample and the platinum tip. The effect of the heater was controlled to keep the temperature difference between the silicon and the platinum cantilever at a constant, and a potential difference was applied to cancel the current from the Seebeck effect so that $I_{\text{total}} = 0$.

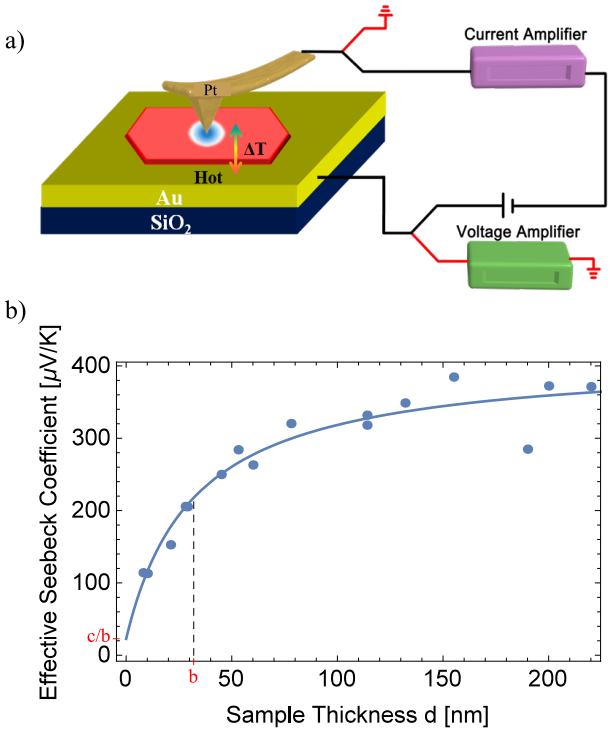

FIGURE 2.1: a) Schematic illustration showing the experimental setup done in Beijing. The red layer is the BDT crystal. b) Measured effective Seebeck coefficient against the layer thickness. Each point represents an experimental setup. The experimental data is fitted to eq. (2.2) with values $S_{s,\text{fit}} = 413\mu\text{V/K}$, $b_{\text{fit}} = 32\text{nm}$ and $c_{\text{fit}} = 724\ \text{nm}\cdot\mu\text{V/K}$.

This was done for many BDT samples of different thickness, and the effective Seebeck coefficient $S_{\text{eff}} = -\Delta V/\Delta T$ was measured in each case. S_{eff} refers to the Seebeck coefficient of the setup as a whole. In other words, the temperature might drop in the gold layer or the tip, and the thermopower of these will contribute to ΔV. Thus, the experiment is not a direct measure of the desired BDT sample. Furthermore as discussed in section 1.3 regarding open circuit measurements, there is also a temperature drop in the connecting experimental setup which also contributes to the measured potential difference. S_{eff} is therefore a measure of the STM setup relative to the connecting circuit with an unknown S_{circuit}.

The experimentally obtained S_{eff} is plotted as a function of the thickness d in figure 2.1b. From the data points and the fitted line which will be discussed further down, we see that S_{eff} starts out at some small value $\sim 20\frac{\mu V}{K}$ for very thin samples. It then increases with the thickness until it saturates at $\sim 400\frac{\mu V}{K}$.

We now want to examine whether this characteristic length dependence is a property of the experimental setup rather than quantum effects in the molecule layer and investigate if the Seebeck coefficient can be deduced from S_{eff}.

2.1.1 The Circuit Model

Our first approach to this question will be to describe each material region through a thermal conductivity, an electrical conductivity and a Seebeck coefficient. The three-dimensional shape of each region is reduced to 1D-component specified by a cross section

area and a length. The heat transfer path is then described as components in series connected as shown to the right in fig. 2.2. It is assumed that there is no temperature drop across the silicon wafer which is reasonable due to its macroscopic cross section area and high thermal conductivity. Additionally the surrounding atmospheric air is considered to be thermally insulating, which is a crude approximation, but we will return to this later. From eq. (1.23), the Seebeck coefficient of serial connected components is:

$$S_{\text{eff}} = \frac{S_s R_{q,s} + S_{\text{Au}} R_{q,\text{Au}} + S_{\text{tip}} R_{q,\text{tip}} + S_{\text{Pt}} R_{q,\text{Pt}}}{R_{q,s} + R_{q,\text{Au}} + R_{q,\text{tip}} + R_{q,\text{Pt}}} \tag{2.1}$$

$$= \frac{S_s d + c}{d + b} \ , \tag{2.2}$$

where the subscript s refers to the BDT sample and d is the sample thickness. The constants b and c are defined as:

$$\begin{aligned} b &= \kappa_s A_s \left(R_{q,\text{Au}} + R_{q,\text{tip}} + R_{q,\text{Pt}} \right) \\ c &= \kappa_s A_s \left(S_{\text{Au}} R_{q,\text{Au}} + S_{\text{tip}} R_{q,\text{tip}} + S_{\text{Pt}} R_{q,\text{Pt}} \right) \ . \end{aligned} \tag{2.3}$$

Remember that the S_{eff} is measured relative to S_{circuit} of the connecting circuit as discussed in section 1.3. S_s is therefore not directly the Seebeck coefficient of the sample. We will neglect S_{circuit} for now to make the discussion simpler. In the limit of thick samples $d \to \infty$, the model in eq. (2.2) yields $S_{\text{eff}} \to S_s$. This is quite intuitive, since we expect the main temperature drop to be across the sample in this limit. Consequently the sample is the only thermopower contributor and the measured Seebeck coefficient should be that of the sample. For very thin samples $d \to 0$ the model yields $S_{\text{eff}} \to c/b = \frac{S_{\text{Au}} R_{q,\text{Au}} + S_{\text{tip}} R_{q,\text{tip}} + S_{\text{Pt}} R_{q,\text{Pt}}}{R_{q,\text{Au}} + R_{q,\text{tip}} + R_{q,\text{Pt}}}$. The measured Seebeck coefficient is thus that of the serial connected components without a sample, which again agrees with the intuition.

When the experimental data is fitted to the model in (2.2), we get the values $S_{s,\text{fit}} = 413 \mu\text{V/K}$, $b_{\text{fit}} = 32$ nm and $c_{\text{fit}} = 724$ nm$\cdot\mu$V/K. The fitted line is plotted with the data in fig. 2.1b and we see that the model resembles the data pretty well. The b value indicates the thickness at which S_{eff} is half-way between the values $S_{\text{eff}}(d = 0)$ and $S_{\text{eff}}(d \to \infty)$ as indicated on the figure. The c-value defined in eq. (2.3) contains information about Seebeck coefficients of the setup. Due to the unknown S_{circuit}, it is not easy to model as will become clear in the following.

The dimensions of the actual experimental setup were provided by our Chinese collaborators and presented in table 2.1. It should be mentioned that we only received a rough estimate on the dimensions, since the exact dimensions are not easy to obtain. From these values we now want to calculate the b- and c-values and see if the fitted values can be reproduced. In reality the tip is curved and the center part might be squished into the molecular layer. The outer part of the tip contact region is close enough to the sample to allow for heat transfer through air, but we will neglect this for now. We approximate the tip-sample contact area to be a circle with a radius of 30 nm.

The dimensions in table 2.1 and the material constants from table 1.1 are now inserted into the circuit model. The thermal resistance of the tip is calculated as a truncated cone $R_{\text{q,tip}} = \frac{h_{\text{tip}}}{\pi \kappa_{\text{Pt}} r_{\text{tip,small}} r_{\text{tip,large}}}$. The obtained c-value is ~ 2 nm$\cdot\mu$V/K and thus way off compared to the fitted value. Part of the explanation is the unknown S_{circuit}, since

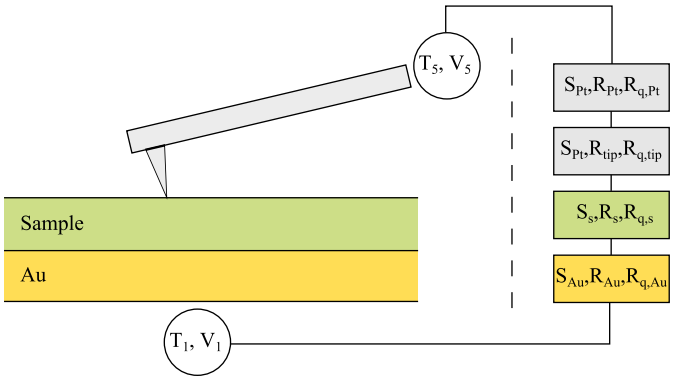

FIGURE 2.2: Schematic illustration of the experimental setup to the left. Model with serial connected components to the right.

the result does not improve as we improve the model. We will therefore not present the c-values.

The resulting b-value is 2200 nm and thus a factor of 70 off compared to the fitted values as shown in table 2.2. The main reasons for this bad result are that the model neglects the constriction resistance close to the sample-tip contact and the heat conduction through air. We will start to improve the model by investigating the constriction resistance using the FEM method.

2.1.2 Thermal Constriction Resistance

The biggest problem about the presented simple model is that it neglects the constriction resistance when going from the sample with a macroscopic cross section area to the tip on the nanoscale. In order to investigate this constriction resistance, we start by calculating the temperature configuration of the setup.

The heat equation for the experimental setup is solved using the technique described in section 1.5.1. This homogeneous technique is in general not true for inhomogeneous setups, but I use it here for reasons that will become clear in chapter 3. The heat equation is only solved in a small region around the sample layer for several reasons: The exact dimensions of the setup are not known, the calculation of the complete setup would be too demanding, and the main temperature drop takes place around the contact between the sample and the tip. A reduced region allows us to use cylinder symmetry since we do not include the cantilever. The material constants ascribed to each material region and the change between two material regions is set as step functions. On the top and bottom boundaries we enforce Dirichlet bc (fixed temperature) and on the sides we require zero heat flux (Neumann bc). For simplicity, the surrounding air was at first considered insulating (Neumann bc).

The interesting part of the resulting temperature map is shown in figure 2.3. We see that the actual temperature change only occurs in a small squeezed hemisphere in the sample layer when compared to the $4\,\mu\text{m}^2$ cross-section area of the sample. The simplification in the first simple model, that the sample is a component with the cross-section area $4\,\mu\text{m}^2$ is therefore obviously invalid, and this is the main reason for the huge derivation.

TABLE 2.1: Estimated dimension for the experimental setup shown in fig. 2.1a. (*) Cross section area of sample-tip contact. The tip has a 15 degree angle.

Material	Length [μm]	Cross-section area [μm^2]
Au	0.03	4
Organic crystal	d	4
Pt	400	12
Tip	60	$\pi \cdot 0.03^2$ (*)

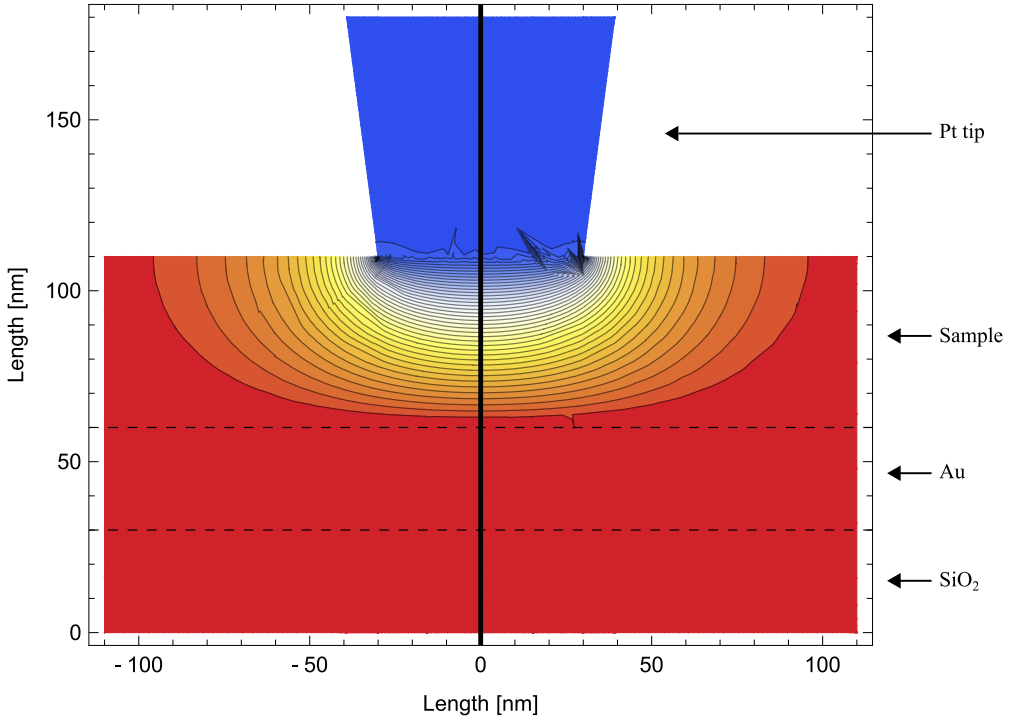

FIGURE 2.3: Cross sectional temperature map of the setup with sample thickness $d = 50$ nm obtained by solving the heat equation. Cylindrical symmetry is used. The dashed lines indicate a border between two materials. Starting from the bottom: silicon, gold, BDT sample and a platinum tip.

Based on the temperature maps for several sample thicknesses, we initially guessed that the thermal resistance of the sample layer could be approximated by a cylinder with radius $r_{\text{s,eff}} = 100$ nm. Substituting this into the simple model in (2.3), we obtained $b = 17$ nm which is in good agreement with the fitted value $b_{\text{fit}} = 32$ nm. However this was nothing but a guess.

To improve the model, we therefore want to include the thermal constriction resistance associated with the contact between the sample and the tip. To do so, I performed a FEM calculation on the sample layer alone with the tip contact area as one Dirichlet boundary, and the bottom as the other. By calculating on the sample alone, the thermal resistance can be calculated and included in the model on the form (2.1). The thermal resistance was calculated for many different sample thicknesses d by $R_{\text{q,s,calc}}(d) = \Delta T / I_{q,\text{calc}}(d)$ where the heat current is:

TABLE 2.2: b-values obtained from different model approaches: Fitted to experimental data, simple circuit model and the circuit model including constriction resistance.

	b [nm]
Fitted values	32
Circuit model calculation	2.2×10^3
Circuit model with constriction resistance	1.3

$$I_{q,\mathrm{calc}}(d) = -2\pi\kappa_\mathrm{s} \int_0^{R_\mathrm{s}} dr \cdot r \cdot \frac{\partial T_d}{\partial z} \ . \tag{2.4}$$

Here T_d is the temperature configuration for a sample of thickness d. Assuming that only the sample resistance depends on thickness, the simple model (2.1) is:

$$S_{\mathrm{eff,simple,constric}}(d) = \frac{S_s R_{q,s,\mathrm{calc}}(d) + S_\mathrm{Au} R_{q,\mathrm{Au}} + S_\mathrm{tip} R_{q,\mathrm{tip}} + S_\mathrm{Pt} R_{q,\mathrm{Pt}}}{R_{q,s,\mathrm{calc}}(d) + R_{q,\mathrm{Au}} + R_{q,\mathrm{tip}} + R_{q,\mathrm{Pt}}} \ . \tag{2.5}$$

In order to compare this new model including the thermal constriction resistance to the experimental results, I fitted the calculated data points to eq. (2.2) and obtained $b = 1.3$ nm. This is an improvement to the simple model, but yet a factor of 25 off compared to the experimental results as shown in table 2.2. Nevertheless the calculation indicates that the constriction resistance plays an important role. For thin samples, there is also a thermal constriction resistance in the Au and SiO_2 layers which would lead to a larger b-value. This will effectively be included in the following section.

For further improvement, we therefore need to include more materials in the FEM calculation and to take heat conduction of the surrounding air into account.

2.1.3 Heat Conduction Through Air

In an attempt to reproduce the experimental results, a FEM calculation including air conduction was done. Instead of the homogeneous procedure, the technique decribed in section 3.3.2 was used. The calculation was done for many sample sizes and the Seebeck coefficient was obtained from the calculated potential difference and the enforced temperature difference $S = -\Delta V/\Delta T$. The resulting temperature map is plotted in fig. 2.4a for sample thickness $d = 50nm$.

Even though this calculation includes a larger part of the tip and the ambient, it does not improve the results compared to the simple model including constriction resistance. It is actually worse since the macroscopic connecting parts are not included and they play an important role in the b-value. I tried to use the calculated region in fig. 2.4a as a new thermoelectric component and connect it to the circuit through the serial model, but that did not improve the result either. From the discussion in the following we will understand that this is as far as we get with numerical modeling.

In order to illustrate how small the calculated part is, the setup is sketched in its proper proportions in fig. 2.4b. Zooming in (for the pdf-version) the gold and sample thicknesses can be compared to the rest of the setup and the region in fig. 2.4a is marked with a

dashed red line. From this perspective, it is obvious that only a small part of the heat conduction through the air is included in the calculation. In principle the whole region in fig. 2.4b could be included, but this would be a very difficult numerical calculation in which the dimensions of all the components should be known in detail.

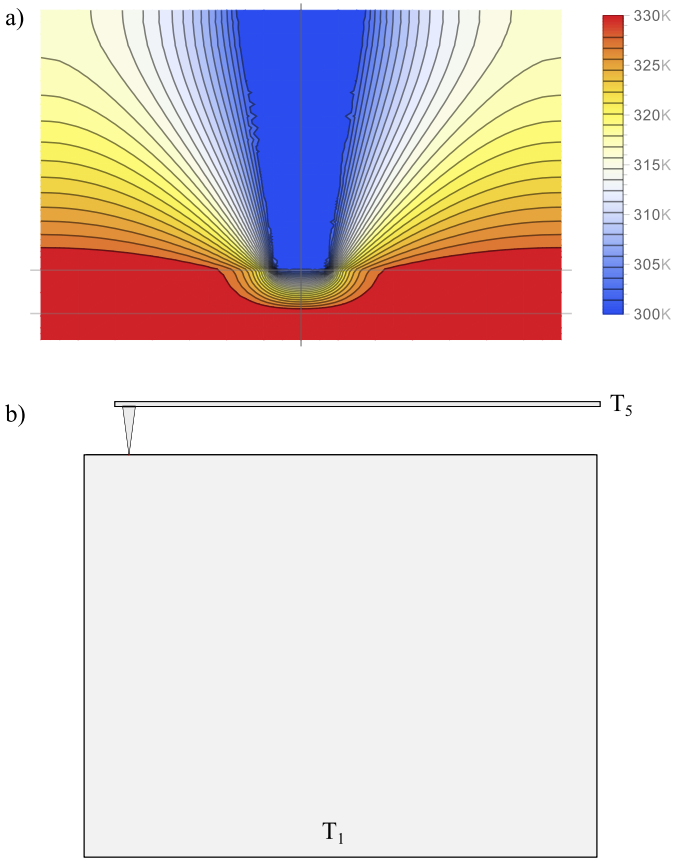

FIGURE 2.4: a) Temperature map obtained using the inhomogeneous procedure presented in sec 3.3.2. Sample thickness $d = 50$ nm and heat conductivity $\kappa_{\text{air}} = 0.024 \frac{\text{W}}{\text{m K}}$ were used. b) The setup in its right proportions. The calculated region in (a) is marked with a dashed red line (zoom in). The horizontal width of the Si and Au layers is unknown.

Figure 2.4b illustrates that the tip and cantilever is surrounded by a large volume of air, which can transport heat. Heat conduction by air lowers the temperature drop across the sample and therefore affects the generated thermopower. S_s is consequently not the Seebeck coefficient of the sample as indicated by the circuit model. It is not easy to include the air conduction in a circuit model since there are many contributions going from: sample to tip, Au to tip, Au to cantilever, SiO_2 to tip and SiO_2 to cantilever. These contributions depend on pressure and humidity, and are therefore unknown.

2.2 Discussion

For the experiment on length dependent thermopower, we have described the experimental results using a simple model of components in series. When the constriction resistance was included, the obtained b-value was a factor of 25 off compared to the experimental results. Further inclusion of the ambient close to the sample-tip contact

did not improve the result. There are many sources of error in these model calculations of which the most important are:

- The numerical calculations are sensitive to the sizes of the macroscopic components and the shape of the tip. We only have a rough estimate on these details.
- Heat conduction through air affects the measurement, but it is not easy to include in neither a model nor a FEM calculation due to many unknowns such as dimensions, pressure and humidity.
- The Seebeck coefficient is measured against S_{circuit} which is unknown.
- The tip-sample contact area depends on the exact shape of the tip. Here it is approximated as a perfect circle with radius 30 nm.
- It is assumed that there is no temperature drop in the silicon, which lowers the b-value.
- The material constants are approximated to change abruptly when going from one material to the other. In reality, smooth transitions occur which plays an important role for thin samples in particular.
- The constants b and c in the simple model are proportional to the thermal conductivity of the BDT crystal, which is unknown (see table 1.1).

Thus, there are many sources of error which affect the results. In a review article on scanning thermal miroscopy from 2015 [15], Gomes *et al.* points out this challenge: "*The estimation of all the involved parameters through modelling is not trivial and is still one of the main limitations of SThM involving nanoprobes*". Involved parameters refer to material properties of the sample, tip-sample contact, ambient pressure, ambient humidity, etc. In order to obtain material properties such as the Seebeck coefficient of the sample, the article points out that calibration is the key [15]. I.e. a compound with known material properties is measured prior to an unknown compound. From the first measurement the sources of error are subtracted so that the Seebeck coefficient can be obtained in the second measurement. We did not look further into this experimental calibration.

Even though the calculations are inaccurate, the macroscopic model reproduces the same line shape as the experimental results. This indicates that the observed length dependence is caused by the experimental setup rather than a quantum effect in the molecular level. Nevertheless, we did not investigate any length dependence of the Seebeck coefficient of the sample, but we do not expect this to be significant. We will return to this in section 4.2.2, where we consider length dependence in single molecule.

In the process of obtaining temperature and potential maps of the tip setup, simple inhomogeneous setups were considered. In these calculations I discovered the existence of electric current density loops under the zero net current condition. This interesting effect will be the topic for the rest of the thesis.

In summary, we reproduced the line shape of the experimental data on thickness dependent thermopower. The calculated result was a factor of 25 off compared to the experimental results due to the many unknowns and sources of error. We conclude that the model is evidence that the length dependence is a result of the experimental setup.

Chapter 3

Thermopower in Inhomogeneous Systems

We have now set up the FEM procedure to calculate temperature and electrical potential fields and used it on the inhomogeneous experimental setup in the precious chapter. However, the homogeneous calculation procedure does not hold for inhomogeneous setup in general, as indicated in the introductory chapter. In this chapter we will build an understanding on when and why the procedure holds and a procedure for calculating inhomogeneous setups is presented. We will use an example system to illustrate how the problem was discovered and solved.

As we will see, the reason for the errors in the homogeneous-procedure is that internal electric currents are flowing, even though the net current is zero. Retrospectively, this is quite intuitive since such currents existed in the original experiment by Seebeck in fig. 1.1. After I (the author) realized and solved the problem, I became aware that the effect was already discussed in the literature as thermoelectric Eddy currents. These have been discussed in the circuit model [16], for a closed inhomogeneous setup [17], and under current flowing conditions where the net current was substracted [18]. Inverse problems of thermoelectricity have also been studied, where the material composition and Eddy currents are known, and the result is the temperature field [19]. To my knowledge, the procedure for solving inhomogeneous open systems under the "$I = 0$" condition is not described in the literature.

3.1 Ill-behaved Electrical Potential Field

In this section we will calculate the temperature and electrical potential fields of an inhomogeneous setup using the homogeneous procedure described in section 1.5.1. The result is evaluated and it is proven that the procedure invalid for the particular setup.

Consider the simple setup shown schematically in figure 3.1a. A small gold cylinder is placed inside a larger aluminum cylinder. The material constants are defined in table 1.1 and the change in space from gold to aluminum is set as a smooth step function in the material constants. Following the homogeneous procedure described in section 1.5.1, the top and bottom boundaries are set to 290 K and 300 K (Dirichlet bc), while the curved side of the outer cylinder is set to be thermally insulating (Neumann bc).

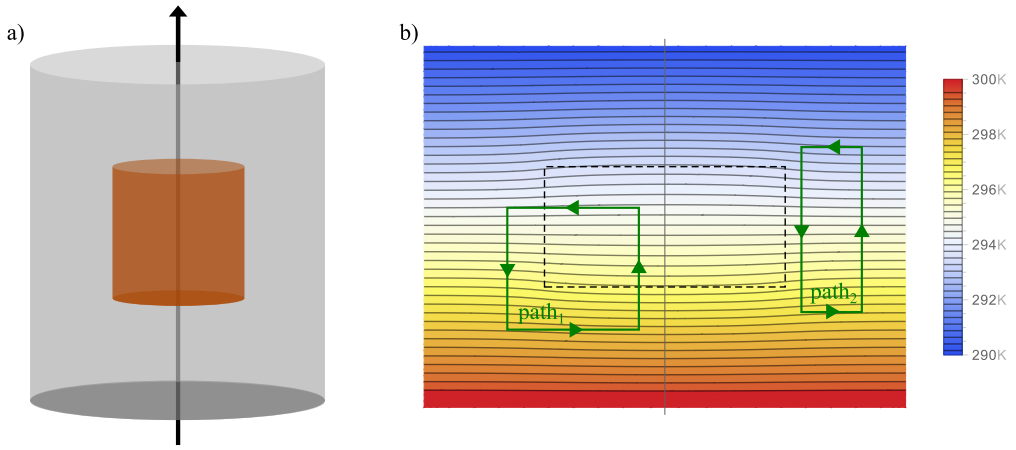

FIGURE 3.1: a) Schematic illustration of the cylinder-in-cylinder example with a small Au cylinder placed inside a larger Al cylinder. b) The cross-sectional temperature map obtained from the homogeneous-procedure using the finite element method. The dashed line indicates the border between the two materials and the green paths are used for discussion in the text.

The solution to the boundary value problem of the heat equation $\nabla \cdot (\kappa(\boldsymbol{r})\nabla T(\boldsymbol{r})) = 0$ is shown in figure 3.1a as a cross-sectional temperature map. The dashed line indicates the border between the two materials. The solution is a well-behaved temperature field so any closed loop line integral inside the volume satisfies $\oint \nabla T(\boldsymbol{r}) \cdot dl = 0$.

As described in section 1.5.1, the potential map can be obtained from a line integral of the gradient $\nabla V = -S\nabla T$. For the technique to be correct, we should obtain a well-behaved electrical potential field, so that any closed-loop integral would equal zero. Consider now the two closed paths path_1 and path_2 shown in fig. 3.1b. The integrals for these two paths yield:

$$\oint_{\text{path}_1} S(\boldsymbol{r})\nabla T(\boldsymbol{r}) \cdot dl \neq 0 \ , \tag{3.1}$$

$$\oint_{\text{path}_2} S(\boldsymbol{r})\nabla T(\boldsymbol{r}) \cdot dl = 0 \ . \tag{3.2}$$

When crossing the material border, we thus get the unphysical result that the electric field is non-conservative. The homogeneous technique of calculating the potential field configuration is therefore incorrect for this inhomogeneous setup. Nevertheless, it is mentioned as "the exact S calculation" in recent literature [20] and it is used by several groups to describe inhomogeneous setups [20–22].

As indicated in section 1.2.1, the error is due to the misassumption that the electric current density vanishes everywhere in the setup. We will see how this appears from the fundamental transport equations in the following section.

3.2 Internal Currents under Conditions I=0

From the experimental condition that the total current is set to zero $I = 0$ it is assumed that the same holds for the local current density $\boldsymbol{J}_e = 0$. This assumption is made in

modern condensed matter textbooks [1, 3] where only the local equations are considered and similarly in recent articles [20–22] where it is used as input in FEM calculations. But as pointed out in the previous section, the assumption is wrong.

The existence of internal currents is easily understood when the cylinder setup in fig. 3.1a is thought of as two components in a parallel setup. In the parallel circuit model presented in section 1.3, internal current loops appear under this the $I = 0$ condition. The existence a local current densities also appear when considering the electric transport equation:

$$\boldsymbol{J}_e(\boldsymbol{r}) = -S(\boldsymbol{r})\sigma(\boldsymbol{r})\nabla T(\boldsymbol{r}) - \sigma(\boldsymbol{r})\nabla V(\boldsymbol{r}) \ . \tag{3.3}$$

If we divide this equation by the electrical conductivity, take the curl and remember that the curl of a gradient is zero, we get:

$$\nabla \times \left(\frac{\boldsymbol{J}_e}{\sigma} \right) = -\left(\nabla S\right) \times \left(\nabla T\right) \tag{3.4}$$

Notice that this equation is independent of the electrical potential. In the case where the $S(\boldsymbol{r})$-profile of an inhomogeneous experimental setup is such that ∇S is perpendicular to the temperature gradient, the right hand side is non-zero. Consequently the electric current density must be non-zero for conducting samples. Likewise, when the gradient of the Seebeck coefficient is parallel to the temperature gradient, the current density will vanish. This result will also become clear with the procedure to be developed in section 3.3.2.

Equation (3.4) thus indicates that electric current densities can exist independent of the applied potential difference. The next step is to calculate these currents.

3.3 Solution to Inhomogeneous Setups

In the previous section we argued that internal current densities can exist in Seebeck measurements of inhomogeneous setups. In order to calculate the exact currents, we have to reconsider the treatment of the transport equations. In the first place, the choice of equations and boundary conditions was not easy. I came up with two procedures to calculate the potential field configuration and the internal currents. The first is complicated and computationally demanding, while the second is simple and fast.

3.3.1 First Procedure

The procedure in this section is rather tedious and only the important thoughts are outlined. For the reader who wants to know how the problem is solved in a simple manner, jump to the next section.

Briefly, the idea of the first procedure is as follows: The electric current is split into a "curl current" and a "gradient current": $\boldsymbol{J}_e = \nabla \times \boldsymbol{A}_e + \nabla \chi_e$, where $\boldsymbol{A}$ is a vector field and χ_e is a scalar field. Taking the curl of the current and using Coulomb gauge

for $\boldsymbol{A}$, an expression for A can then be found using the Greens function technique. By taking the curl of $\boldsymbol{A}$, the "curl-current" takes the form as a non-local integral where the complicated integrand depends on the temperature and potential field configurations.

With this formulation, the solution follows from iterating over the following steps:

1. Solve the heat equation, which includes the electric current density from the second iteration
$$\nabla \cdot \Big[-\tilde{\kappa}\nabla T + TS\boldsymbol{J}_e \Big] = 0 \tag{3.5}$$
2. Calculate the "curl-current" with the temperature field (1) and potential field (4) as input.
3. Calculate the "gradient current" from the $\nabla^2\chi = 0$ boundary value problem, using the Neumann boundary condition $\boldsymbol{J}_e = 0 \Rightarrow \nabla\chi_e = -\nabla \times \boldsymbol{A}_e$. This ensures that the current density disappears on the boundaries (with (2) as input).
4. Calculate the potential gradient field $\nabla V = -S\nabla T - \frac{\boldsymbol{J}_e}{\sigma}$

The iterative process is done when closed loop line integrals of the potential gradient yields a number of the same order as the numeric noise. This procedure assumes that the current density vanishes at all boundaries. This is not necessarily true, but it plays an insignificant role when the $(\nabla S) \times (\nabla T) \neq 0$ region is far away from the boundaries.

The non-local integration when calculating the "curl current" is computationally demanding and the procedure is very technical. In the following section we will see a more elegant approach.

3.3.2 Second Procedure

The procedure of this section is inspired by the experimental detail of the Seebeck measurement. The experimentalist applies a temperature difference to a component in a circuit. Due to the thermoelectric effect, the component responds with an electric current. The experimentalist then tunes an applied potential difference so that $I = 0$ and we will now do the same theoretically.

Consider again the two transport equations (1.4) and (1.5). Inserting these into the steady-state continuity equations $\nabla \cdot \boldsymbol{J}_q = 0$ and $\nabla \cdot \boldsymbol{J}_e = 0$, we get:

$$0 = \kappa\nabla^2 T + \nabla\kappa \cdot \nabla T + TS\sigma\nabla^2 V + T\nabla(S\sigma) \cdot \nabla V \ , \tag{3.6}$$
$$0 = S\sigma\nabla^2 T + \nabla(S\sigma) \cdot \nabla T + \sigma\nabla^2 V + \nabla\sigma \cdot \nabla V \ , \tag{3.7}$$

where the second order term with $(\nabla T)^2$ has been neglected. We thus have a set of coupled differential equations for each spatial dimension. Consider again the cylinder-in-cylinder setup in fig. 3.1a as an example. Inspired by the experiment, we use Dirichlet bc to the top and bottom to keep a fixed temperature difference $T_2 - T_1$ and a potential difference $V_{\text{test}} - V_1$ across the component. The boundary conditions are

$$\begin{aligned} &\text{Bottom: } T = T_1,\ V = V_1 \\ &\text{Side: } \frac{\partial T}{\partial r} = 0,\ \frac{\partial V}{\partial r} = 0 \\ &\text{Top: } T = T_2,\ V = V_{\text{test}} \end{aligned} \tag{3.8}$$

With these boundaries, we solve the coupled equations (3.6) and (3.7) simultaneously using the finite element method. As a result we get the temperature and potential field configuration inside the component from which we can calculate the electric current density, $\boldsymbol{J}_e = -S\sigma\nabla T - \sigma\nabla V$. The net current through the setup is then calculated by integrating up the current density at the circuit-connected boundary. In the case of a cylinder with radius R the current is:

$$I_{\text{test}} = 2\pi \int_0^R dr\ r \left(-\kappa \frac{\partial T}{\partial z} - TS\sigma \frac{\partial V}{\partial z} \right) . \tag{3.9}$$

Inspired by the experimentalist, we want to tune the applied potential difference so that this net current vanishes. We therefore change V_{test} while keeping the other boundaries in 3.8 fixed, and do another FEM calculation. Again the current is calculated, and from linear regression a potential V_2 is found so that the total current is zero. Analogously to the Seebeck experiment, we have thus tuned the potential difference to ensure the condition $I = 0$.

For the cylinder-in-cylinder example, the temperature map is plotted in figure 3.2a. This correct temperature map is very similar to the result obtained from the homogeneous procedure in fig. 3.1b. The obtained potential field configuration is plotted in figure 3.2b. In contrast to the result from the homogeneous procedure, the potential is uniquely defined in every point inside the cylinders. The sharp edges on some of the isopotential lines are due to numeric noise from the finite element method.

The electric current density can now be calculated by inserting the obtained temperature and potential gradient fields into the transport equation (1.5). The result is shown in figure 3.2c. We see that current actually does flow at the circuit-connected edges, but it sums up to zero on the complete edge as required. In other words, only closed loop currents are formed and some of these loops stretch into the connecting leads. The current loops flow around the material intersections at which $\nabla S \times \nabla T \neq 0$ which is in agreement with our previous arguments. It e.g. explains why the line integral along path_1 in fig. 3.1b is non-zero.

The electric current loops will induce a magnetic field. In this cylinder-setup the magnetic field lines will be in the angle direction and most intense close to the material intersection. It would therefore be difficult to measure the magnetic field, and we will not calculate it in this case. Another example is given in section 3.5, where the magnetic field is calculated and discussed.

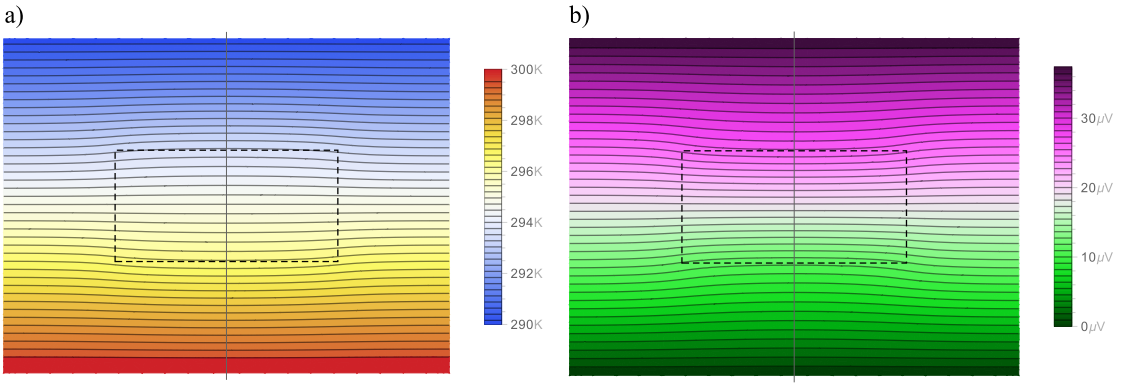

FIGURE 3.2: Cross-sectional results for the cylinder-setup shown schematically in fig. 3.1. The results include the temperature field configuration (a), the potential map (b) and the electric current densities (c). The dashed line marks the border between the two materials.

3.4 Charachterization of the Results

Continuing with the cylinder-in-cylinder example, we now want to examine the results from the new calculation procedure. We will see how the internal currents depend on the material composition and how the calculated Seebeck coefficient of the component deviates from a standard calculation.

From the circuit consideration in eq. (1.22) and the reduced transport equation in eq. (3.4), we argued that the internal currents vanish when the gradient of the Seebeck coefficient is zero or parallel to the temperature gradient. Additionally the current around a material junction is expected to vanish if one of the materials does not conduct electric current. We now want to verify these predictions with the developed numerical procedure and examine the dependence of the internal currents on the material constants.

Consider the cylinder-in-cylinder setup shown in fig. 3.3a. The big cylinder is defined with the material constants of aluminum while the and small cylinder has values S_{small} and σ_{small}. Following the description in section 3.3.2, the potential difference canceling the net current was found, and the loop currents were calculated by integrating up the electric current density along the red path in fig. 3.3a. I then looped over different values of S_{small} and σ_{small} repeating the described procedure in each case. At this point

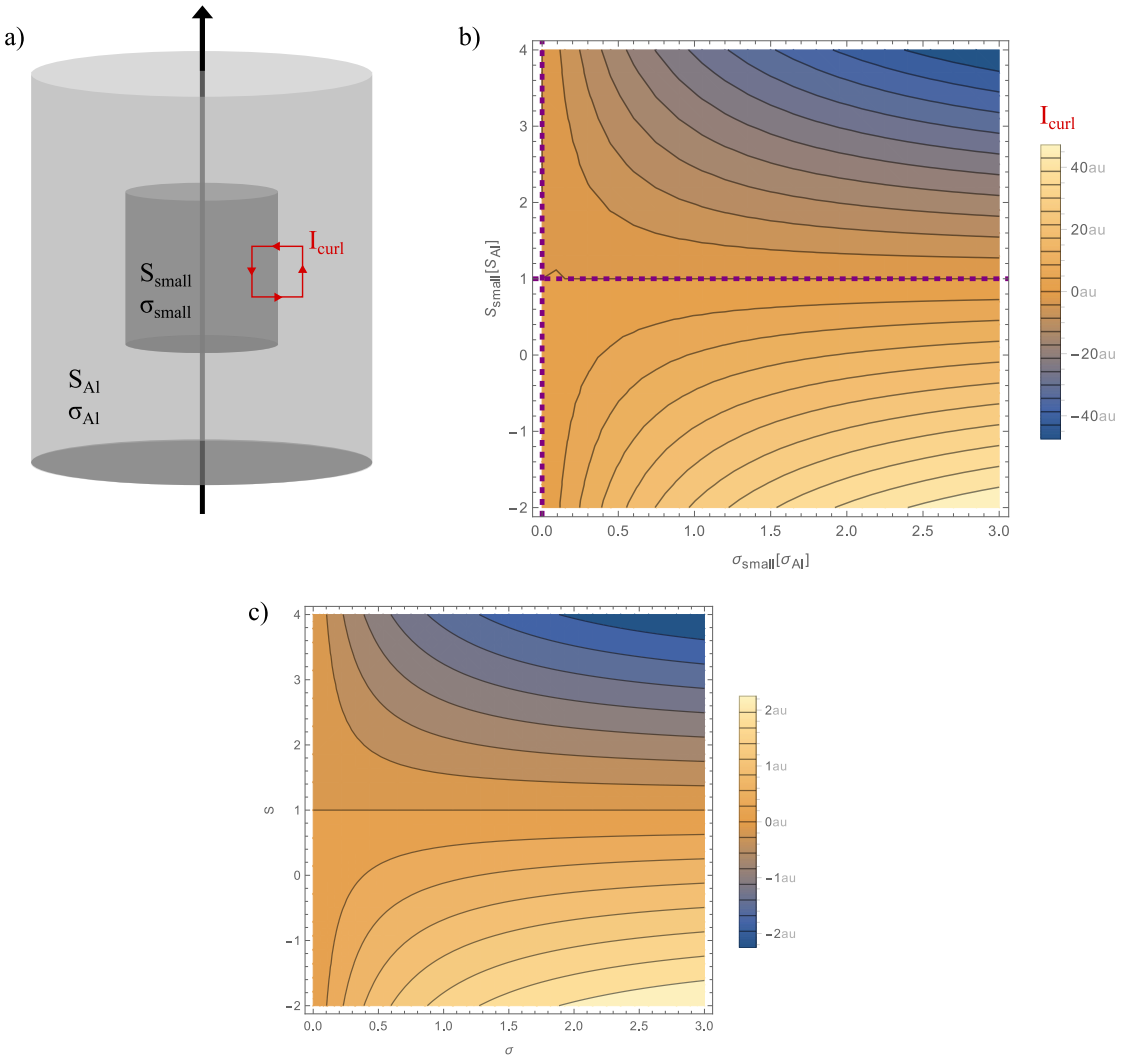

FIGURE 3.3: a) Cylinder-in-cylinder setup with varying Seebeck coefficient S_{small} and electrical conductivity σ_{small} in the small cylinder. The loop-current is calculated by integrating along the red path. b) Loop currents for different material compositions calculated using the FEM method. The dashed purple line indicates compositions where $I_{\text{curl}} = 0$. c) Loop currents calculated from the reduced circuit model eq. (3.10). The currents are in arbitrary units.

we do not care about the actual intensity of the currents, as they depend on the actual size of the cylinders and the integration path.

This was done for more than 450 material compositions, and the calculated loop currents are plotted in fig. 3.3b. Here σ_{small} is along the x-axis in units if σ_{Al} while S_{small} is along the y-axis in units of S_{Al}. The horizontal dashed line thus represents the material compositions at which the Seebeck coefficient is constant $S_{\text{small}} = S_{\text{Al}}$ inside the whole setup. Similarly the vertical dashed line are the cases in which $\sigma_{\text{small}} = 0$. The results show that the internal currents are zero for the material compositions along these lines, just as predicted from the parallel circuit model, $I_{\text{loop,parallel}} = \frac{S_1 - S_2}{R_1 + R_2}\Delta T$ in (1.22). To compare, we set $S_1 = \sigma_1 = 1$ and neglect the dimension dependence $R \sim 1/\sigma$ so that the loop current in eq. (1.22) can be expressed as:

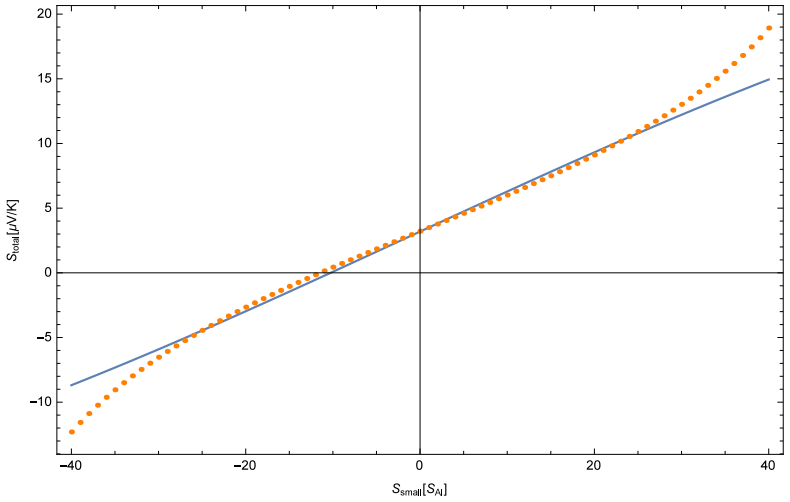

FIGURE 3.4: The total thermopower of the cylinder-in-cylinder component in fig. 3.3a. The temperature difference is $\Delta T = 1$ K and $S_{\mathrm{Al}} = 3.5\mu\mathrm{V/K}$. The blue line is calculated from the circuit model, while each orange dot is from a FEM calculation.

$$I_{\mathrm{loop,parallel}} \sim \frac{\sigma}{\sigma + 1}(1 - S) \ . \tag{3.10}$$

This expression for the circuit model loop current is plotted in fig. 3.3c. We see great similarities between fig. b and c, and thus the internal current loops in this cylinder-in-cylinder component can be understood from the parallel circuit model. The influence of the thermal conductivity was also studied, but it did not affect the internal currents.

We will now investigate how the Seebeck coefficient of the cylinder-in-cylinder component is affected by the internal currents. The correct Seebeck coefficient is obtained from the FEM results as the ratio between the applied potential and temperature differences, $S = -\frac{\Delta V}{\Delta T}$. For comparison, the setup is considered as parallel connected components of Au and Al with the resulting Seebeck coefficient, $S_{\mathrm{parallel}} = \frac{S_{\mathrm{Al}}\tilde{R}_{\mathrm{q,Al}} + S_{\mathrm{Al\text{-}Au}}R_{\mathrm{q,Al\text{-}Au}} + S_{\mathrm{Al}}\tilde{R}_{\mathrm{q,Al}}}{\tilde{R}_{\mathrm{q,Al}} + R_{\mathrm{q,Al\text{-}Au}} + \tilde{R}_{\mathrm{q,Al}}}$. The parallel thermal resistance $R_{\mathrm{q,Al\text{-}Au}}$ is here a long expression which can be derived from the equations in section 1.3.

The results are shown in fig. 3.4 where the blue line is from the circuit calculation while each orange dot is the result of a FEM calculation. In the homogeneous case where $S_{\mathrm{small}} = S_{\mathrm{Al}}$, we know that there is no internal currents and intuitively both calculations yield $S_{\mathrm{total}} = S_{\mathrm{Al}}$. For differences in the Seebeck coefficients between the two materials of around $100\mu\mathrm{V/K}$ ($\sim 30S_{\mathrm{Al}}$) we see only small divination in the two calculation procedures. For most commonly used metals, S only varies around $10\mu\mathrm{V/K}$ and the influence of the internal currents is here insignificant [6]. On the other hand, semiconductors have larger variations in Seebeck coefficients, and here the procedure of calculation influences the result more significantly. Remember that the developed FEM procedure yields the correct thermopower, not the circuit calculation.

In this section we showed that internal current loops in a cylinder-in-cylinder setup could be understood from the parallel circuit model. With this knowledge, we will now set up an example of an experimental setup in which the currents could be detected.

3.5 Example: Gated Graphene

One way to detect the existence of internal current loops experimentally is to measure the magnetic field. To obtain a setup from which the magnetic field lines point out, we now turn away from cylinder symmetry. In the spirit of nanoscience, we will discuss an example of internal loop currents in graphene.

Graphene is a sheet of sp^2 hybridized carbon atoms. Due to its one-atom-thickness of 0.34 nm it can be considered as a two-dimensional material. It has gained a lot of attention in the field of physics and nanotechnology e.g. due to its high thermal and electrical conductivities.

One way to turn the homogeneous graphene into an inhomogeneous 2D material is to add a top gate. The gate voltage affects the carrier density in the graphene level and thereby alters the transport properties. The exact values have been found experimentally to be $\sigma = 0.1$ mS and $S = 0$ for ungated graphene, while a -10 V gate changes the values to $\sigma = 0.4$ mS and $S = 70\ \frac{\mu V}{K}$ [23]. Measuring the thermal conductivity is still an active research area and different research groups do not agree on the exact value. For the calculations in this chapter we use $\kappa_{3D} = 2000\frac{W}{m\,K}$ which gives the two-dimensional thermal conductivity $\kappa_{2D} = 0.34\text{nm} \cdot 2000\frac{W}{m\,K} = 6.8 \cdot 10^{-7}\frac{W}{K}$.

From the knowledge build up in the previous sections, we need $\nabla S \times \nabla T \neq 0$ for internal currents to appear. For the currents to be as large as possible, we place a $1\mu m \times 1\mu m$ gate on top of a $2\mu m \times 3\mu m$ graphene sheet so that the gradients are perpendicular to each other as shown schematically in fig. 3.5a. We define the gated and ungated material constants on this geometry with smooth material boundaries and solve equations (3.6) and (3.7) using the FEM procedure. The boundary conditions are as indicated in the figure. Notice that the problem is very similar to the cylinder-in-cylinder example, but this time the equations are solved for 2D cartesian coordinates.

The resulting electric current densities are shown in fig. 3.5b, where the gated region is marked with dashed lines. Again we observe closed current loops circulating the line at which $\nabla S \times \nabla T$. Some of the loops stretch into the contacts but the contributions on either the upper or lower boundary adds up to zero. To illustrate the intensities of the currents, the y-component along the center of the graphene sheet is plotted in fig. 3.5c, where we see that the maximum current density is around $17\frac{nA}{\mu m}$.

To calculate the order of magnitude of the magnetic field in the center of the loops, the Biot-Savart law for a conducting loop is used: $B = \frac{\mu_0 I}{2R}$. The current densities are condensed into a single ring with radius $R = 0.5\mu m$ and the total current $I = 1\mu m \cdot 12nA/\mu m = 12nA$. The magnetic field pointing in the -z direction is then calculated to be $B \sim 10^{-8}T$. Modern magnetometers can measure fields on the sub-nano scale and it would therefore be possible to detect the electric current loops experimentally. Notice that the current densities scale with the sample size. If we e.g. chose the graphene sheet to be one tenth the size of the one in fig. 3.5a (200nm × 300nm), the current density would be $\sim 120nA/\mu m$. In the simple Biot-Savart ring, the current would again be 12 nA, on consequently the magnetic field $B \sim 10^{-7}T$.

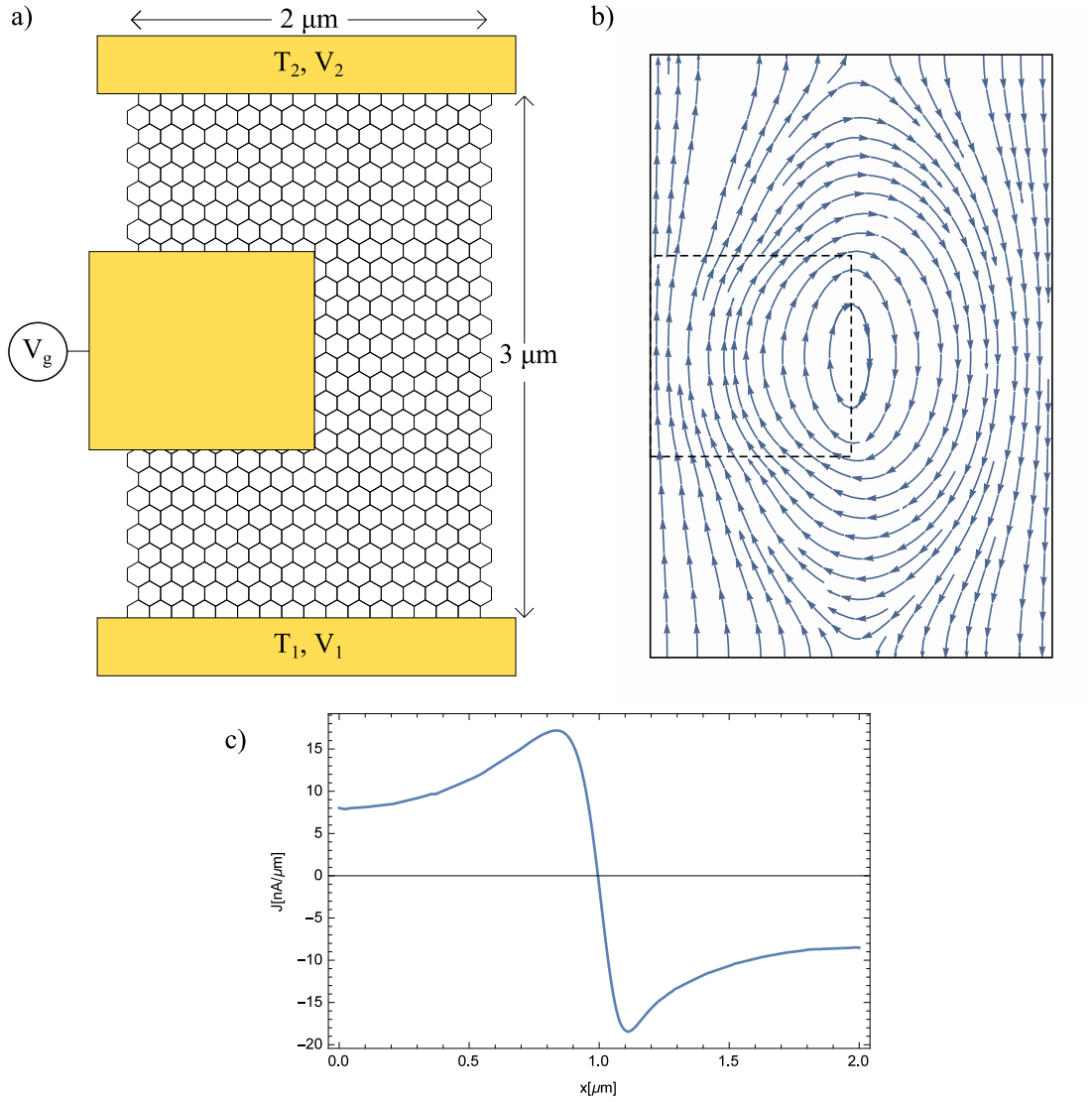

FIGURE 3.5: a) Schematics of top-gated graphene. Notice that the graphene structure is enlarged. b) The calculated electric current densities. c) The y-component of the electric current density through the middle cross section.

3.6 Final Remarks

In this chapter we have argued that electric current loops exist under the zero net current condition and provided a procedure of calculation. For a simple setup, different material compositions were investigated and it was shown that if $\nabla S \times \nabla T \neq 0$, internal currents exist. As an example, top-gated graphene was considered and it was shown that induced magnetic fields were of an experimentally detectable strength.

In chapter 2, we initially used the homogeneous procedure to investigate the experimental setup. Even though the setup was inhomogeneous, the calculation procedure does not play a significant role since the main temperature drop is parallel to the change in material constants, $\nabla S \times \nabla T \sim 0$. The resulting loop currents are therefore very small compared to the perpendicular case in the cylinder setup of this chapter. The same holds for modern thermoelectric generators as depicted in fig. 1.5b where $\nabla S \times \nabla T = 0$.

Chapter 4

Introduction to Transport in Single Molecules

Until this point we have studied macroscopic systems using classical field theory. We have shown that internal current loops appear when solving the linear transport equations with the correct boundary conditions. From this discovery, our hypothesis is that similar currents exist in molecules. We therefore need to investigate transport on a molecular scale and we will turn to the tools from quantum mechanics. In this chapter the field of single molecule transport and measurements in general are introduced. Length dependent Seebeck coefficients in single molecules are then discussed in the light of the experiment in chapter 2.

4.1 Single Molecule Measurements

Before going to the theoretical consideration on transport in single molecules, we will briefly discuss the experimental challenges associated with single molecule (SM) measurements. In the experiment on length dependent Seebeck coefficients in chapter 2, the AFM tip was in contact with many BDT molecules in the organic crystal at the same time. The BDT crystal was stable and had a large surface area compared to the tip area, so getting a Au-molecules-tip connection was fairly easy.

Doing a SM measurement is in general more challenging. The molecules are normally in solution and therefore without a fixed position. They are small and more than one molecule can bind between two contacts so that the SM character of the measurement is spoiled. The setups used for SM measurements are normally formed by breaking thin metal junctions into two contacts [24]. In a scanning tunneling microscopy (STM) break junction [25] for example, a metal tip is forced into contact with a metal coated substrate and pulled back up until the formed junction breaks, which is observed in a conductance measurement. After the breakage, the contact distance can be controlled very precisely.

The molecules of interest are prepared with binding groups, so that they bind to the metal contacts. A thiol is an example of a binding group that forms strong Au-Sulfur bonds. The molecules are either deposited onto or in solution with the break junction contacts, so that they bind to the metal surfaces. By measuring the conductance while changing the contact distance, a situation where only a single molecule connects the

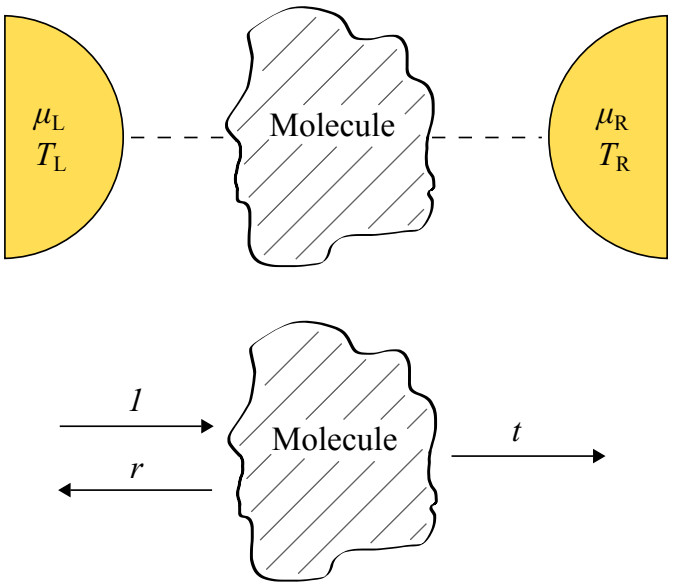

FIGURE 4.1: Top: Schematics of an arbitrary molecule trapped between two contacts. Each contact is thermalized with the shown temperature and chemical potential. Bottom: Transport through the molecule can be considered as the quantum mechanical barrier problem.

contacts can be obtained. The junction breakage is then done thousands of times and the traces showing SM characteristics are selected for further analysis.

This section indicates that single molecule setups are dynamic and complicated from an experimental point of view. From now on we will turn to the theoretical consideration which is more clean and simple. We will start by describing the electric current and Seebeck coefficient in the single particle picture.

4.2 Single Particle Picture

We will now look at the electron transport in molecules within the single particle picture. In this picture the contacts shown in the top fig. 4.1 are assumed to be two independent and incoherent electron reservoirs, i.e. the electrons in the left (right) contact is in thermal equilibrium and Fermi distributed at temperature and chemical potential T_L and μ_L (T_R and μ_R). The molecule is considered as a barrier at which an electron coming from the left reservoir can be reflected with amplitude r or transmitted into the right reservoir with amplitude t as seen in the lower fig. 4.1. The transport is assumed elastic so that an incoming electron with energy E has the same energy after being reflected or transmitted, and it thermalizes in the reservoir in which it is absorbed. The current through such a system is given by the Landauer formula [26]:

$$I_{L\to R} = \frac{e}{\pi\hbar}\int_{-\infty}^{\infty} dE\, \mathcal{T}(E)\left[f_R(E) - f_L(E)\right] \ , \tag{4.1}$$

where $\mathcal{T}(E)$ is the so-called transmission function, which expresses probability of being transmitted at energy E. The technical details in single molecule transport are mostly

concerned with obtaining $\mathcal{T}(E)$, from which the zero-temperature conductance and the Seebeck coefficient follow. From the scattering picture in fig. 4.1, the transmission function is $\mathcal{T}(E) = |t(E)|^2$. Using the transfer matrix formalism, we will derive the Landauer formula in section 5.3.1. First we will see how the Seebeck coefficient is connected to the transmission function.

4.2.1 Seebeck Coefficient

With the Landauer formula as a starting point, an expression for the Seebeck coefficient in the single particle picture can be derived [27]. By expanding the Fermi functions to linear order under the assumption that the bias and temperature difference between the contacts are small:

$$f_{\mathrm{R}}(E) - f_{\mathrm{L}}(E) = -\frac{\partial f(E,\mu,T)}{\partial E}\left[e\Delta V + \frac{\Delta T}{T}(E-\mu)\right] . \tag{4.2}$$

Assuming low temperature and no temperature difference, the conductance $G = \frac{e^2}{\pi\hbar}\mathcal{T}(\mu)$ is obtained, when the expansion is inserted into the Landauer equation (4.1). Without these assumptions on the temperature, we can find an expression for the Seebeck coefficient $S = -\frac{\Delta V}{\Delta T}$ under the condition $I = 0$:

$$S(T) = -\frac{1}{eT}\frac{\int_{-\infty}^{\infty} dE\, \mathcal{T}(E)(E-\mu)(-f'(E)))}{\int_{-\infty}^{\infty} dE\, \mathcal{T}(E)(-f'(E)))} . \tag{4.3}$$

When considering low temperatures, the derivative of the Fermi function turns into a delta function, $(-f'(E)) = \delta(E-\mu)$. The denominator is therefore $\mathcal{T}(\mu)$ and the numerator can be expanded using the Sommerfeld expansion (chapter 16, [1]):

$$\int dE\ (-f'(E))\mathcal{T}(E)(E-\mu) = \frac{\pi^2}{3}(k_B T)^2 \frac{d\mathcal{T}(E)}{dE}\Big|_{E=\mu} . \tag{4.4}$$

Inserting these into the expression for the Seebeck coefficient, we get

$$S(T) = -\frac{\pi^2 k_B^2}{3e}\cdot T \cdot \frac{d\ln[\mathcal{T}(E)]}{dE}\Big|_{E=\mu} . \tag{4.5}$$

When the transmission function is known, the Seebeck coefficient can therefore easily be calculated using eq. (4.5).

The Landaur formula and the expression for the Seebeck coefficient only involves the net current through the molecular. As for the calculation of the Seebeck effect using classical field theory, the literature does not pay any attention to the local currents within the molecule. In other words, it is assumed that the local currents are zero everywhere in the molecule. In the chapter 5 we will develop the theory to calculate such currents and we will discover the existence of bond currents under the zero net current condition.

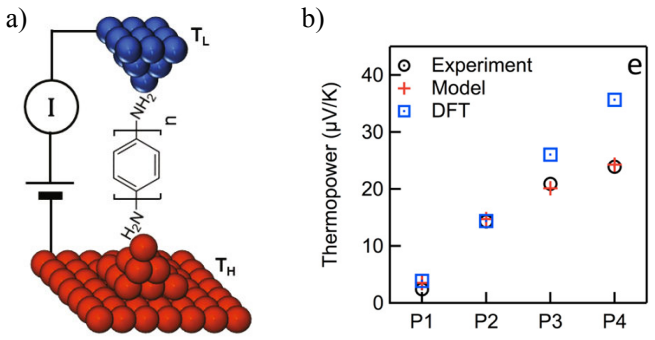

FIGURE 4.2: STM break junction measurements on oligophenylenes. a) Schematics of the experimental setup [28]. b) Measured Seebeck coefficient as a function of the number of phenyls, including calculated values using both DFT and a tight binding model [29].

4.2.2 Length Dependent Seebeck Coefficient in Molecules

In chapter 2, we discussed the experimental results of length dependent thermopower in organic crystals. We concluded that the length dependence was a result of the experimental setup rather than a feature on the molecular level. That being said, very similar length dependencies show up when considering single molecules using the theory just presented. One of the most studied compounds is oligophenyl, for which the Seebeck coefficient has been investigated as a function of the number of para-benzenes.

Several oligophenylene experiments have been done using the STM break junction [28–30] as shown schematically in fig. 4.2a. As described earlier, such a measurement involves thousands of traces from which the ones showing single molecule behavior are selected. The experimental mean values of the Seebeck coefficient as a function of molecule length are shown in fig. 4.2b. The results are supported by calculations done using equation (4.5), where the transmission function was found using both DFT and a tight binding model.

We see that the single molecule Seebeck coefficient as a function of length has a similar shape as the Seebeck coefficient for the organic crystal in figure 2.1b. In order to estimate whether similar effects could play a role in the discussed experimental setup in chapter 2, we want to compare the b-values from the model equation (2.2). The length of a phenyl is ~ 4.2 Å and the experimental curve in fig. 4.2b saturates around 25 $\frac{\mu V}{K}$. The b-value, that describes the length at which the curve is halfway between the starting and saturation value is read off to be ~ 8 Å. This length is thus very small compared to $b = 32$ nm in the BDT measurement.

The BDT and oligophenylene experiments are not directly comparable. For the BDT sample, the number of intermolecular bonds changes with length, while the number of intramolecular bonds changes with length in oligophenylene. Nevertheless, the quantum effects seem to influence the thermopower within a few nanometers, and for the BDT experiment, we expect the changes to be small compared to the effect from experimental setup as described in chapter 2. An intermolecular hopping model could be used to study the effect, but this is yet to be done.

Chapter 5

Thermoelectrically Driven Currents in Molecules

In the previous chapter, the general equations for the conductance and Seebeck coefficient of molecules were discussed. These equations only focus on the net current through molecules, but based on our discovery of internal currents under the condition $I = 0$ in chapter 3, our hypothesis is that the same result will show up in molecules. We will start by introducing the transfer matrix formalism from which we derive the molecular wave function of arbitrary molecules, and then calculate local currents between atom sites. In section 5.4 we will present the interesting result of current loops in ring structured molecules.

5.1 Tight Binding and Transfer Matrix Formalism

The task of this section is to develop the theory needed to calculate local currents within an arbitrary conjugated molecule. We do this using the tight binding (TB) model, also known as the Hückel method. Here π-electron molecular orbitals are described as linear combinations of atomic orbitals:

$$|\Psi\rangle = \sum_n \phi_n |n\rangle \ , \tag{5.1}$$

where $|n\rangle$ is the atomic orbital for atom n, while ϕ_n is the coefficient describing the amplitude on atom n. The Hückel Hamiltonian describing the molecule is:

$$H_{\mathrm{TB}} = \varepsilon_0 \sum_i c_i^\dagger c_i - t \sum_{<ij>} \left(c_i^\dagger c_j + c_j^\dagger c_i \right) \ , \tag{5.2}$$

where $< ij >$ indicates that the sum is over atom sites that are connected by chemical bonds. The annihilation operator c_i removes an electron from site i while the creation operator $c_i^\dagger$ creates an electron at site i. ε_0 is the on-site energy while t is the positive hopping energy. To describe the electron dynamics of the Hückel Hamiltoians we will

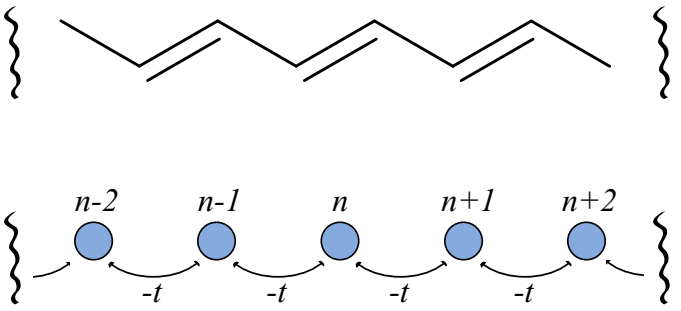

FIGURE 5.1: Top: Section of long conjugated molecule. Lower: An illustration on how the molecule is treated as a string of connected sites, when using the Hückel method

use the transfer matrix formalism. As a first example we consider a long unbranched chain of atoms.

5.1.1 Transfer Matrix of Simple Chain

In this section we will describe the simplest case in the transfer matrix formalism, namely an unbranched chain of atoms. This will later be used to model the contacts in single molecule calculations.

Consider the unbranched conjugated molecule depicted in the top figure 5.1. We consider it infinitely long, so that the energy spectrum becomes continuous and so that edge effects can be neglected. In the Hückel method, each atom is considered as a site and electrons can hop between neighboring sites with an amplitude $-t$ as shown in the lower figure 5.1. In matrix form, the Hamiltonian and the energy eigenvector are

$$\boldsymbol{H}_{\text{string}} = \begin{pmatrix} \varepsilon_0 & -t & 0 & 0 & \\ -t & \varepsilon_0 & -t & 0 & \cdots \\ 0 & -t & \varepsilon_0 & -t & \\ 0 & 0 & -t & \varepsilon_0 & \\ & \vdots & & & \ddots \end{pmatrix} \qquad \boldsymbol{\Psi}_{\text{string}} = \begin{pmatrix} \vdots \\ \phi_{n-1} \\ \phi_n \\ \phi_{n+1} \\ \vdots \end{pmatrix} . \tag{5.3}$$

The eigenvalue problem $\boldsymbol{H}_{\text{string}}\boldsymbol{\Psi}_{\text{string}} = E\boldsymbol{\Psi}_{\text{string}}$ is now a system of linear equations with as many equations as atom sites. The one equation involving the coefficients ϕ_{n-1}, ϕ_n and ϕ_{n+1},

$$(E - \varepsilon_0)\phi_n = -t\left(\phi_{n-1} + \phi_{n+1}\right) , \tag{5.4}$$

can be put into the form

$$\begin{pmatrix} \phi_{n+1} \\ \phi_n \end{pmatrix} = \begin{pmatrix} -\frac{E-\varepsilon_0}{t} & -1 \\ 1 & 0 \end{pmatrix} \begin{pmatrix} \phi_n \\ \phi_{n-1} \end{pmatrix} \tag{5.5}$$

$$\equiv \boldsymbol{T}_{\text{string}}(E) \begin{pmatrix} \phi_n \\ \phi_{n-1} \end{pmatrix} , \tag{5.6}$$

where $\boldsymbol{T}_{\text{string}}$ is defined as the energy dependent transfer matrix for the string. As the name indicates, $\boldsymbol{T}_{\text{string}}$ transfers us from one set of coefficient in the chain to another set. The advantages of this form is that we can easily get any coefficients if we know just ϕ_n and ϕ_{n-1}. The transfer matrix is simply applied the desired number of times:

$$\begin{pmatrix} \phi_{n+a} \\ \phi_{n-1+a} \end{pmatrix} = \boldsymbol{T}^a_{\text{string}}(E) \begin{pmatrix} \phi_n \\ \phi_{n-1} \end{pmatrix} , \tag{5.7}$$

where a is an integer that functions as a matrix power on the right hand side. Since we are going to use a string to model the contacts connecting a molecule in the next section, we are interested in the propagating modes of the string. These modes must be eigenstates of the transfer matrix with eigenvalues that do not decay the mode. The eigenvalues of the transfer matrix are:

$$\lambda_\pm = -\frac{E-\varepsilon_0}{2t} \pm i\sqrt{1-\left(\frac{E-\varepsilon_0}{2t}\right)^2} . \tag{5.8}$$

If we first consider the energies in the range $-2t < E - \varepsilon_0 < 2t$, the eigenvalues can be put into a simpler form by introducing the dimensionless wave number k, which relates to the energy in the following way

$$E'(k) = E - \varepsilon_0 = -2t\cos(k) , \tag{5.9}$$

where E' is introduced for later use. The eigenvalues and eigenvectors are then:

$$\lambda_\pm = \mathrm{e}^{\pm ik} . \tag{5.10}$$

$$\boldsymbol{\xi}_\pm(k) = \frac{1}{\sqrt{2\mathcal{L}}} \begin{pmatrix} \mathrm{e}^{\pm ik} \\ 1 \end{pmatrix} , \tag{5.11}$$

where $\mathcal{L}$ is the length of the system. In the eigenvectors, the normalization factor is included so that they are normalized on the length $\mathcal{L}$: $\int_0^{\mathcal{L}} dx|\xi|^2 = 1$. The full energy spectrum is included when considering the k-values $[0;\pi]$.

For energies in the range $2t < |E - \varepsilon_0|$ the eigenvalues are $\lambda \sim \mathrm{e}^{\pm\kappa}$, where the dimensionless κ takes real values. These states either decay or grow depending on the moving direction and the sign of $E - \varepsilon_0$, and consequently they cannot be normalized. For a sufficiently long string of atoms, we therefore know that the allowed states are in the energy window $-2t < E - \varepsilon_0 < 2t$ and on the form given in eq. (5.11). As mentioned, the infinite length ensures that the energy spectrum becomes continuous. The chain can therefore be seen as an energy band, $-2t < E - \varepsilon_0 < 2t$, in which electrons travel freely. We will use these chains as electron reservoirs to model the contacts in a single molecule measurement.

We have now considered the unbranched chain of atoms using the transfer matrix formalism and will turn to the case of arbitrary molecules.

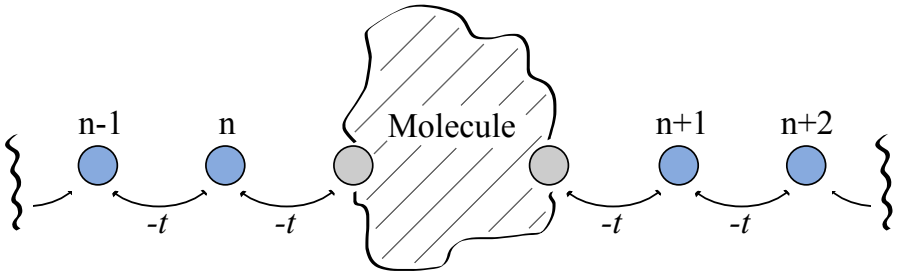

FIGURE 5.2: An arbitrary molecule connected to electron reservoirs modeled as atom chains. The grey sites are part of the molecule.

5.2 Arbitrary Molecules

Until this point the idea of the transfer matrix formalism has been introduced and the unbranched chain of atoms discussed. In this section we will develop the theory to calculate the full wavefunction of an arbitrary molecule. The task of this section is a bit technical and it is split into three parts:

- In section 5.2.1, we derive the transfer matrix for an arbitrary molecule. This allows us to transfer from one lead to the other.
- In section 5.2.2, we connect the scattering problem and the transfer matrix method. In this way, we can calculate the lead coefficients with the transfer matrix as input.
- In secion 5.2.3, we calculate the molecule part of the wavefunction using the coefficients in the left lead as an input.

5.2.1 Transfer Matrix of an Arbitrary Molecule

In this section we will derive a molecule transfer matrix, which takes us from one side of an arbitrary molecule to the other.

If we for example add a side chain to the discussed simple chain, this can effectively be reduced to an unbranched chain with an on-site energy at the branch point [31]. A ring structure such as benzene can also be reduced to an unbranched chain where two sites have on-site energies and are connected by a new hopping amplitude [31]. For more complicated molecules this way of treating the problem becomes inefficient, so instead we will derive the transfer matrix for an arbitrary molecule.

Consider the arbitrary molecule connected to an unbranched chain of atoms as sketched in fig. 5.2. The Hamiltonian for such a problem includes a $\boldsymbol{H}_{\text{string}}$ for each lead as defined in eq. (5.3), the Hamiltonian for the molecule $\boldsymbol{H}_{\text{M}}$ which I will describe shortly, and finally it includes the vectors $\boldsymbol{\Gamma}_\alpha$ and their transposed. The $\boldsymbol{\Gamma}_\alpha$'s describe the coupling between the molecule and chain α, where α is either left or right. If e.g. the left chain is coupled to the atom site 2 on the molecule with amplitude $-t$, the transposed vector $\boldsymbol{\Gamma}_{\text{L}}^T$ is $(0 \quad -t \quad 0 \quad 0 \quad \dots)$. The full Hamiltonian is:

$$\boldsymbol{H} = \begin{pmatrix} \boldsymbol{H}_{\text{string}} & & & \\ & \boldsymbol{\Gamma}_{\text{L}}^{T} & & \\ & \boldsymbol{\Gamma}_{\text{L}} & \boldsymbol{H}_{\text{M}} & \boldsymbol{\Gamma}_{\text{R}} \\ & & \boldsymbol{\Gamma}_{\text{R}}^{T} & \\ & & & \boldsymbol{H}_{\text{string}} \end{pmatrix}, \tag{5.12}$$

where the empty space outside the marked boxes is zeros. For a molecule with N atoms, $\boldsymbol{H}_{\text{M}}$ has dimensions $(N \times N)$ while $\boldsymbol{\Gamma}_{\text{L}}$ and $\boldsymbol{\Gamma}_{\text{R}}$ have dimensions $(N \times 1)$. We only need to include a (2×2) version of $\boldsymbol{H}_{\text{string}}$ as indicated in fig. 5.2, because the remaining coefficients in the connecting leads can be obtained from eq. (5.7).

The molecule Hamiltonian can be obtained in the following way: If atom site i and j in the molecule are connected by a bond, it appears as $\boldsymbol{H}_{\text{M,ij}} = \boldsymbol{H}_{\text{M,ji}} = -t$. All matrix elements for unconnected sites appear as zeros while the diagonal holds is the on-site energy ε_0. To avoid typing errors, the Hamiltonian is usually imported into Mathematica from `www.huckelmethod.com`. To make it more transparent what is hidden in the boxes in eq. 5.12, a para-substituted benzene is here given as an explicit example:

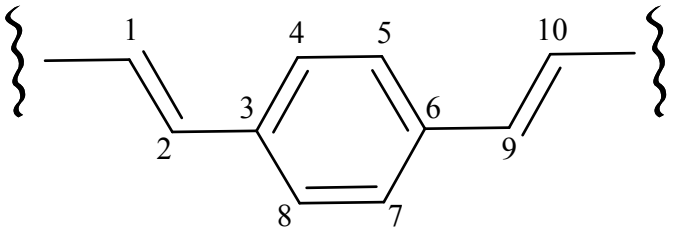

$$\boldsymbol{H}_{\text{benzene}} = -t \begin{pmatrix} \frac{-\varepsilon_0}{t} & 1 & & & & & & & \\ 1 & \frac{-\varepsilon_0}{t} & & & & & & & \\ & & 1 & 0 & 0 & 0 & 0 & 0 & \\ & & 0 & \frac{-\varepsilon_0}{t} & 1 & 0 & 0 & 0 & 1 & 0 & \\ & & 0 & 1 & \frac{-\varepsilon_0}{t} & 1 & 0 & 0 & 0 & 0 & \\ & & 0 & 0 & 1 & \frac{-\varepsilon_0}{t} & 1 & 0 & 0 & 0 & \\ & & 0 & 0 & 0 & 1 & \frac{-\varepsilon_0}{t} & 1 & 0 & 1 & \\ & & 0 & 0 & 0 & 0 & 1 & \frac{-\varepsilon_0}{t} & 0 & 0 & \\ & & 0 & 0 & 0 & 1 & 0 & 0 & & & \\ & & & & & & & & \frac{-\varepsilon_0}{t} & 1 \\ & & & & & & & & 1 & \frac{-\varepsilon_0}{t} \end{pmatrix}, \tag{5.13}$$

where the blank matrix elements are zeros and left out for clarity.

We split the wavefunction into three components with the coefficients in the left lead, the molecule and the right lead:

$$\boldsymbol{\Psi} = \begin{pmatrix} \boldsymbol{\Psi}_{\mathrm{L}} \\ \boldsymbol{\Psi}_{\mathrm{M}} \\ \boldsymbol{\Psi}_{\mathrm{R}} \end{pmatrix} \ . \tag{5.14}$$

If we apply the general Hamiltonian in eq. (5.12) to this wavefunction, we get a linear system with $N+4$ equations. Our task is to derive the transfer matrix, which connects the left side coefficients ϕ_{n-1} and ϕ_n to the right side coefficients ϕ_{n+1} and ϕ_{n+2} in fig. 5.2. I.e. we need to eliminate the coefficients on the molecule so that we are left with the coefficients of interest. Consider the N equations involving the molecule and the two equations involving $\boldsymbol{\Gamma}_{\mathrm{L}}^T$ and $\boldsymbol{\Gamma}_{\mathrm{R}}^T$:

$$\boldsymbol{H}_{\mathrm{M}}\boldsymbol{\Psi}_{\mathrm{M}} + \boldsymbol{\Gamma}_{\mathrm{L}}\phi_n + \boldsymbol{\Gamma}_{\mathrm{R}}\phi_{n+1} = E\boldsymbol{\Psi}_{\mathrm{M}} \tag{5.15}$$

$$\boldsymbol{\Gamma}_{\mathrm{L}}^T\boldsymbol{\Psi}_{\mathrm{M}} - t\phi_{n-1} = (E-\varepsilon_0)\phi_n \tag{5.16}$$

$$\boldsymbol{\Gamma}_{\mathrm{R}}^T\boldsymbol{\Psi}_{\mathrm{M}} - t\phi_{n+2} = (E-\varepsilon_0)\phi_{n+1} \ . \tag{5.17}$$

Remember that the ϕ's are coefficients for the atom sites and the indices are as shown in fig. 5.2. From eq. (5.15) we isolate $\boldsymbol{\Psi}_{\mathrm{M}}$

$$\boldsymbol{\Psi}_{\mathrm{M}} = \boldsymbol{G}\left(\boldsymbol{\Gamma}_{\mathrm{L}}\phi_n + \boldsymbol{\Gamma}_{\mathrm{R}}\phi_{n+1}\right) \ , \tag{5.18}$$

where we introduced the Greens funcion as $\boldsymbol{G} = (E\mathbb{1} - \boldsymbol{H}_{\mathrm{M}})^{-1}$. We now insert this into eqs. (5.16) and (5.17)

$$V_{LL}\phi_n + V_{LR}\phi_{n+1} - t\phi_{n-1} = (E-\varepsilon_0)\phi_n \tag{5.19}$$

$$V_{RL}\phi_n + V_{RR}\phi_{n+1} - t\phi_{n+2} = (E-\varepsilon_0)\phi_{n+1} \ , \tag{5.20}$$

where the introduced V's are defined as $V_{\alpha\beta} \equiv \boldsymbol{\Gamma}_\alpha^T\boldsymbol{G}\boldsymbol{\Gamma}_\beta$. To keep the notation as simple as possible, we will use the notation $E' = E - \varepsilon_0$. From equations (5.19) and (5.20), we isolate the coefficients ϕ_{n+1} and ϕ_{n+2}:

$$\phi_{n+1} = \frac{E'-V_{LL}}{V_{LR}}\phi_n + \frac{t}{V_{LR}}\phi_{n-1} \tag{5.21}$$

$$\phi_{n+2} = -\frac{E'-V_{RR}}{t}\phi_{n+1} + \frac{V_{RL}}{t}\phi_n \tag{5.22}$$

$$= -\frac{1}{t}\left[\left(E'-V_{RR}\right)V_{LR}^{-1}\left(E'-V_{LL}\right) - V_{RL}\right]\phi_n - \left[\left(E'-V_{RR}\right)V_{LR}^{-1}\right]\phi_{n-1} \ . \tag{5.23}$$

We have now obtained two equations with only the coefficients of interest. The equations are now put on the transfer matrix form,

$$\boldsymbol{\Psi}_{\mathrm{R}} = \begin{pmatrix} \phi_{n+2} \\ \phi_{n+1} \end{pmatrix} = \boldsymbol{T}_{\mathrm{M}} \begin{pmatrix} \phi_{n} \\ \phi_{n-1} \end{pmatrix} = \boldsymbol{T}_{\mathrm{M}} \boldsymbol{\Psi}_{\mathrm{L}} \ , \tag{5.24}$$

where the molecule transfer matrix $\boldsymbol{T}_{\mathrm{M}}$ is defined as:

$$\boldsymbol{T}_{\mathrm{M}}(k) = \begin{pmatrix} -\frac{1}{t}\left[(E' - V_{RR})\, V_{LR}^{-1}\, (E' - V_{LL}) - V_{RL}\right] & -(E' - V_{RR})\, V_{LR}^{-1} \\ (E' - V_{LL})\, V_{LR}^{-1} & t V_{LR}^{-1} \end{pmatrix} . \tag{5.25}$$

Equation (5.24) allows us to find the coefficients of the atomic orbitals on one side of an arbitrary molecule by knowing the coefficients on the other side. The only input in $\boldsymbol{T}_{\mathrm{M}}$ is the molecule Hamiltonian $\boldsymbol{H}_{\mathrm{M}}$ and the left and right coupling vectors, $\boldsymbol{\Gamma}_{\mathrm{L}}$ and $\boldsymbol{\Gamma}_{\mathrm{R}}$. Remember that both the explicit E' and the $V_{\alpha\beta}$'s depend on the k-value introduced in eq. (5.9).

One way to test whether $\boldsymbol{T}_{\mathrm{M}}$ gives the correct result is to use an unbranched chain as a molecule. For a chain with B atom sites, the Hamiltonian $\boldsymbol{H}_{\mathrm{string},(B\times B)}$ from eq. (5.3) is used as input and compared with eq. (5.7). It is verified that

$$\boldsymbol{T}_{\mathrm{M}}\left[\boldsymbol{H}_{\mathrm{string},(B\times B)}\right] = \boldsymbol{T}_{\mathrm{string}}^{B+2} \ , \tag{5.26}$$

where $(B+2)$ is a matrix power.

In this section we derived the molecule transfer matrix in eqs. (5.24) and (5.25), which can be used to connect the left and right leads. The coefficients in the leads are yet unknown and it is the task of the following section to calculate these.

5.2.2 Transmission Through an Arbitrary Molecule

In this section we will connect the transmission and reflection amplitudes from scattering theory to the molecule transfer matrix. From this, we get obtain the lead wave functions.

As discussed in section 4.2, we work in the single particle picture where the transmission through the molecular region can be considered as the tunneling problem shown in the bottom figure 4.1. Using chains as leads, the lead wave functions $\boldsymbol{\Psi}_L$ and $\boldsymbol{\Psi}_R$ can be decomposed into the eigenfunctions $\boldsymbol{\xi}_+$ and $\boldsymbol{\xi}_-$ of the transfer matrix. These eigenfunctions are defined in eq. (5.11) and represent right and left propagating modes. If we consider an electron coming from the left, it has amplitudes as shown in the bottom figure 4.1, where the right/left-pointing arrows refer to $\boldsymbol{\xi}_{+/-}$:

$$\boldsymbol{\Psi}_{\mathrm{L}}^{\mathrm{L}}(k) = \boldsymbol{\xi}_{+}(k) + r(k)\boldsymbol{\xi}_{-}(k) \tag{5.27}$$

$$\boldsymbol{\Psi}_{\mathrm{R}}^{\mathrm{L}}(k) = t(k)\boldsymbol{\xi}_{+}(k) \ , \tag{5.28}$$

where the superscript refers to the origin electron reservoir, while the subscript indicates coefficients in either the left or right lead. These equations represent an ordinary scattering problem with t and r as the k dependent transmission and reflection amplitudes.

By the use of the transfer matrix in eq. (5.24), the two equations can be connected in the following way:

$$\boldsymbol{T}_{\mathrm{M}}^{-1}(k)t(k)\boldsymbol{\xi}_{+}(k) = \boldsymbol{\xi}_{+}(k) + r(k)\boldsymbol{\xi}_{-}(k) \ , \tag{5.29}$$

where $\boldsymbol{T}_{\mathrm{M}}^{-1}$ is the inverse transfer matrix. The $\boldsymbol{\xi}_{+}(k)$ with amplitude *1* may carry a complex phase which results in the same phase factor in front of all ϕ's in the total wavefunction. In section 5.3 we will see that the phase does not affect the current and therefore we leave it out. Equation (5.29) can be put into the matrix form,

$$\begin{pmatrix} \boldsymbol{T}_{\mathrm{M}}^{-1}\boldsymbol{\xi}_{+} & -\boldsymbol{\xi}_{-} \end{pmatrix} \begin{pmatrix} t \\ r \end{pmatrix} = \boldsymbol{\xi}_{+} \ , \tag{5.30}$$

where we have suppressed the k-dependence for compactness. The transmission and reflection amplitudes for an electron coming from the left are then:

$$\begin{pmatrix} t \\ r \end{pmatrix} = \begin{pmatrix} \boldsymbol{T}_{\mathrm{M}}^{-1}\boldsymbol{\xi}_{+} & -\boldsymbol{\xi}_{-} \end{pmatrix}^{-1} \boldsymbol{\xi}_{+} \ . \tag{5.31}$$

Analogously, the transmission and reflection amplitudes, t' and r', for an electron coming from the right side are:

$$\begin{pmatrix} t' \\ r' \end{pmatrix} = \begin{pmatrix} \boldsymbol{T}_{\mathrm{M}}\boldsymbol{\xi}_{-} & -\boldsymbol{\xi}_{+} \end{pmatrix}^{-1} \boldsymbol{\xi}_{-} \ . \tag{5.32}$$

With equations (5.31) and (5.32), we are now able to obtain all transmission and reflection amplitudes for an arbitrary molecule. The only input is the transfer matrix $\boldsymbol{T}_{\mathrm{M}}$ which is given by eq. (5.25). And from the transmission and reflection amplitudes we can calculate the lead wave functions. In the left lead, the wave functions are:

$$\boldsymbol{\Psi}_{\mathrm{L}}^{\mathrm{L}}(k) = \boldsymbol{\xi}_{+}(k) + r(k)\boldsymbol{\xi}_{-}(k) \tag{5.33}$$

$$\boldsymbol{\Psi}_{\mathrm{L}}^{\mathrm{R}}(k) = t'(k)\boldsymbol{\xi}_{-}(k) \ , \tag{5.34}$$

where we have reintroduced the k-dependence. The superscripts L and R refer to electrons coming from the left and right reservoir, respectively. Notice that we only considered incoming electrons with the amplitude of unity. Actually the amplitude depends on the distribution in the reservoirs, but we will return to this in section 5.3 when we calculate the currents.

Traditionally the transmission and reflection amplitudes in eqs. (5.31) and (5.32) are represented through the scattering matrix $\boldsymbol{S}$ [32]. From this representation it is easily seen that $|t|^2 = |t'|^2$, and we will therefore discuss it briefly. For the wave functions $\boldsymbol{\Psi}_L = a_+\boldsymbol{\xi}_+ + a_-\boldsymbol{\xi}_-$ and $\boldsymbol{\Psi}_R = b_+\boldsymbol{\xi}_+ + b_-\boldsymbol{\xi}_-$, where the a's and b's are amplitudes, the scattering matrix is defined as:

$$\boldsymbol{c}_{out} = \begin{pmatrix} a_- \\ b_+ \end{pmatrix} = \begin{pmatrix} r & t' \\ t & r' \end{pmatrix} \begin{pmatrix} a_+ \\ b_- \end{pmatrix} = \boldsymbol{S}\boldsymbol{c}_{in} \ . \tag{5.35}$$

From current conservation, the incoming and outgoing probabilities have to equal, $\boldsymbol{c}_{\text{in}}^\dagger \boldsymbol{c}_{\text{in}} = \boldsymbol{c}_{\text{out}}^\dagger \boldsymbol{c}_{\text{out}}$. We therefore have

$$\boldsymbol{c}_{\text{in}}^\dagger \boldsymbol{c}_{\text{in}} - \boldsymbol{c}_{\text{out}}^\dagger \boldsymbol{c}_{\text{out}} = \boldsymbol{c}_{\text{in}}^\dagger \left(1 - \boldsymbol{S}^\dagger \boldsymbol{S}\right) \boldsymbol{c}_{\text{in}} = 0 \ , \tag{5.36}$$

from which we see that the scattering matrix is unitary. From $\boldsymbol{S}^\dagger \boldsymbol{S} = \boldsymbol{S}\boldsymbol{S}^\dagger = \mathbb{1}$ follows the relation $|t|^2 = 1 - |r|^2 = |t'|^2$ which we will use in sec 5.3.1 when deriving the Landauer formula.

In this section we showed how the transmission and reflection amplitudes could be expressed through the molecule transfer matrix. We used this to get the equations (5.33) and (5.33) for the left lead wave function.

5.2.3 Wavefunction on the Molecule

In this section we derive the operator that gives the molecule wave function from the left lead wave function.

With the equations presented in the previous section, we can now transfer from one side of an arbitrary molecule as depicted in fig. 5.2 to the other. The coefficients inside the molecule can be calculated using eq. (5.18). We rewrite this so that we can use the left lead coefficients as a starting point:

$$\boldsymbol{\Psi}_{\text{M}} = \boldsymbol{G}\left(\boldsymbol{\Gamma}_{\text{L}}\phi_n + \boldsymbol{\Gamma}_{\text{R}}\phi_{n+1}\right) \tag{5.37}$$

$$= \boldsymbol{G}\left[\boldsymbol{\Gamma}_{\text{L}} \begin{pmatrix} 1 & 0 \end{pmatrix} \begin{pmatrix} \phi_n \\ \phi_{n-1} \end{pmatrix} + \boldsymbol{\Gamma}_{\text{R}} \begin{pmatrix} 0 & 1 \end{pmatrix} \begin{pmatrix} \phi_{n+2} \\ \phi_{n+1} \end{pmatrix}\right] \ . \tag{5.38}$$

By the use of eq. (5.24) we get

$$\boldsymbol{\Psi}_{\text{M}} = \boldsymbol{M} \begin{pmatrix} \phi_n \\ \phi_{n-1} \end{pmatrix} \ , \tag{5.39}$$

where the molecule matrix $\boldsymbol{M}$ is defined as

$$\boldsymbol{M} = \boldsymbol{G}\left[\boldsymbol{\Gamma}_{\text{L}} \begin{pmatrix} 1 & 0 \end{pmatrix} + \boldsymbol{\Gamma}_{\text{R}} \begin{pmatrix} 0 & 1 \end{pmatrix} \boldsymbol{T}_{\text{M}}\right] \ . \tag{5.40}$$

From equations (5.24) and (5.39) we can now generate the full wave function from the left lead wave function:

$$\boldsymbol{\Psi}(k) = \begin{pmatrix} \boldsymbol{\Psi}_L(k) \\ \boldsymbol{\Psi}_M(k) \\ \boldsymbol{\Psi}_R(k) \end{pmatrix} = \begin{pmatrix} \mathbb{1} \\ \boldsymbol{M}(k) \\ \boldsymbol{T}_{\mathrm{M}}(k) \end{pmatrix} \boldsymbol{\Psi}_L(k) \ , \tag{5.41}$$

where $\boldsymbol{\Psi}_L$ is the two-component vector with coefficients ϕ_n and ϕ_{n-1} defined in eq. (5.33) and (5.34).

5.3 Local Currents in Single Molecule Seebeck Measurements

We have now established the theory to calculate the complete wavefunction for an arbitrary molecule in a junction. In this section we will derive an expression for the bond currents.

Based on our discovery of non-vanishing internal currents in inhomogeneous Seebeck measurements in chapter 3, our hypothesis is that internal currents appear in molecules as well. With the complete wave function, we now have enough information to calculate the local currents between neighboring atom sites. As a starting point, we need to find an expression for the bond current operator.

The bond current operator can be obtained by considering the change in the charge density operator $\hat{\rho}$ on an atom site. Written in the Heisenberg picture, the charge density operator for an arbitrary site n is $\hat{\rho}_n(t) = -e \cdot (c_n^\dagger c_n)(t) = -e \cdot \mathrm{e}^{iHt/\hbar}\, c_n^\dagger c_n\, \mathrm{e}^{-iHt/\hbar}$, where H is the Hamiltonian of the system. Taking the derivative with respect to time,

$$\frac{\partial}{\partial t}\hat{\rho}_n(t) = -\frac{ie}{\hbar}\left[H, c_n^\dagger c_n\right] \ , \tag{5.42}$$

where $[\cdot\,,\cdot]$ is a commutator. For tight binding Hamiltionans of the form (5.2), we derived the necessary relation $\left[c_i^\dagger c_j, c_n^\dagger c_n\right] = c_i^\dagger c_j\,(\delta_{jn} - \delta_{in})$. The change in charge density is connected to the currents via the continuity equation $\frac{\partial}{\partial t}\rho = -\nabla \cdot j$. If we consider a small volume around the atom site n, we can use the divergence theorem to show that

$$\frac{\partial}{\partial t}\hat{\rho}_n(t) = -\sum_{m \,\in\, \text{neighbors}} \hat{j}_{nm} \ , \tag{5.43}$$

where the sum is over neighboring sites, i.e. sites m that are connected to site n by a chemical bond. $\hat{j}_{nm}$ gives the current from site n to site m. Comparing eqs. (5.42) and (5.43) for any tight binding Hamiltonian $H = H_{\mathrm{TB}}$, we get the following expression for the bond current operator:

$$\hat{j}_{nm} = \frac{iet}{\hbar}\left(c_n^\dagger c_m - c_m^\dagger c_n\right) \ , \tag{5.44}$$

where t is the hopping amplitude from H_{TB}. This operator can now be used on the wavefunctions defined in eq. (5.41). The current from site n to site m carried by the mode k is found by taking the expectation value of the operator with respect to $\mathbf{\Psi}(k)$:

$$J_{nm}(k) = \langle \Psi(k) | \hat{j}_{nm} | \Psi(k) \rangle \ . \tag{5.45}$$

Until this point we have assumed that the incoming modes have the amplitude of unity. But since the electrons come from a reservoir, the amplitudes depend on whether the k-state in the reservoir is occupied. In reservoir α, the electrons are distributed according to the Fermi function f_α:

$$f_\alpha(k) = \frac{1}{\exp\left(\frac{E-\mu_\alpha}{k_B T_\alpha}\right) + 1} \tag{5.46}$$

$$= \frac{1}{\exp\left(\frac{E'(k)-(\mu_\alpha-\varepsilon_0)}{k_B T_\alpha}\right) + 1} \ , \tag{5.47}$$

where we added and subtracted ε_0 to the energy and used eq. (5.9). We see that the k-dependent distribution function depends on the chemical potential relative to the on-site energies in the molecule. The chemical potentials of the reservoirs can be controlled by an applied bias while the on-site energy in theory can be controlled by a gate. The total current from site n to site m is found by summing up the contributions from both left and right coming states at all k-values in the window $0 \leq k \leq \pi$:

$$J_{nm} = 2 \sum_k \left(J^L_{nm}(k) + J^R_{nm}(k) \right) \tag{5.48}$$

$$= 2 \sum_k \left(f_L(k) \left\langle \Psi^L(k) \right| \hat{j}_{nm} \left| \Psi^L(k) \right\rangle + f_R(k) \left\langle \Psi^R(k) \right| \hat{j}_{nm} \left| \Psi^R(k) \right\rangle \right) \ , \tag{5.49}$$

where the superscripts refer to the direction from which the electrons are incoming. The factor of two is introduced because each k-state can be occupied by two electrons with opposite spin orientation. In order to get a more explicit expression, we insert eq. (5.44) for the bond current operator. For clarity we change the notation $c^\dagger_m c_n \to |m\rangle \langle n|$ so that $\langle \Psi^\alpha(k)|m\rangle \langle n|\Psi^\alpha(k)\rangle = \int_0^{\mathcal{L}} dx \ \phi^*_m(\alpha,k) \ \phi_n(\alpha,k)$. Here $\phi^*_m(\alpha,k)$ is the complex conjugate of the amplitude on site m for an electron incoming from reservoir α in mode k. We furthermore change the sum to an integral $\sum_k \to \frac{1}{\pi} \int_0^\pi dk$ to get the expression:

$$J_{nm} = i\frac{2et}{\hbar} \sum_{\alpha=L,R} \frac{1}{\pi} \int_0^\pi dk \ f_\alpha(k) \Big(\langle \Psi^\alpha(k)|n\rangle \langle m|\Psi^\alpha(k)\rangle - \langle \Psi^\alpha(k)|m\rangle \langle n|\Psi^\alpha(k)\rangle \Big) \tag{5.50}$$

$$= \frac{4et}{\pi\hbar} \mathcal{L} \sum_{\alpha=L,R} \int_0^\pi dk \ f_\alpha(k) \ \mathrm{Im}\left[\phi^*_m(\alpha,k) \ \phi_n(\alpha,k)\right] \ . \tag{5.51}$$

This final equation is used in Mathematica to calculate the bond currents. In section 5.4 we will discuss the results of different chemical compounds defined. The length $\mathcal{L}$ is not

important, since it is canceled by the $\mathcal{L}^{-1/2}$ in the ϕ's. As discussed earlier, the incoming electrons can carry a phase, which results in a phase factor in front of all coefficients. From eq. (5.51) we see that such a phase would cancel and therefore not influence the currents.

In this section we derived an expression (5.51) to calculate bond currents in an arbitrary molecule. This expression is used to derive the Landauer formula in the following section and to calculate internal currents under the $I = 0$ condition in section 5.4.

5.3.1 Total Current through Single Molecules

In this section we derive an expression for the total current through a molecule and intuitively arrive at the Landauer formula.

Equation (5.51) for the bond currents depends on the temperatures and chemical potentials of the electron reservoirs via the Fermi functions. For a Seebeck measurement we have to find the potential difference required to insure $I = 0$ for a given temperature difference $\Delta T = T_R - T_L$. We do this by calculating the total current through the molecule, i.e. the bond current between the atom sites $n-1$ and n in figure 5.2.

The ϕ's for electrons coming from the left and right are obtained from equations 5.33 and 5.34, respectively, where $\mathbf{\Psi}^{\alpha}_{\mathrm{L}}(k) = \begin{pmatrix} \phi_n(\alpha, k) \\ \phi_{n-1}(\alpha, k) \end{pmatrix}$. Inserting the propagating modes from equation 5.11, the imaginary parts in eq. (5.51) evaluate to:

$$\mathrm{Im}\left[\phi_n^*(L,k)\,\phi_{n-1}(L,k)\right] = -\frac{1}{2\mathcal{L}}\left(1-|r(k)|^2\right)\sin k \tag{5.52}$$

$$\mathrm{Im}\left[\phi_n^*(R,k)\,\phi_{n-1}(R,k)\right] = \frac{1}{2\mathcal{L}}|t'(k)|^2\sin k\ . \tag{5.53}$$

The probability of transmission is collected as the transmission function, $\mathcal{T} = |t|^2 = 1-|r|^2 = |t'|^2$, where the last step follows from the unitarity of the S-matrix as discussed in section 5.2.2. Inserting these imaginary parts into eq. (5.51), we get the total current

$$J_{n-1,n} = \frac{2et}{\pi\hbar}\int_0^{\pi} dk\ \sin(k)\mathcal{T}(k)\left[f_R(k) - f_L(k)\right]\ . \tag{5.54}$$

Since the energy is defined as in eq. (5.9), we can rewrite $dk = dE'\left(\frac{dE'}{dk}\right)^{-1} = \frac{dE'}{2t\sin k}$. We therefore recover the Landauer formula in eq. (4.1) when doing a change of variables. This verifies the derived expression for the bond currents in eq. (5.51).

In the following section, we want to calculate bond currents under the condition that the total current is zero, i.e. the Seebeck measurement condition. For predefined temperatures and chemical potential T_L, T_R and $\mu_L - \varepsilon_0$, the Landauer formula is set to zero and solved numerically to find μ_R. Alternatively, the chemical potential difference could be calculated from eq. (4.5), but the numerical calculation is chosen, so that all bond currents are calculated in the same way.

5.4 Results

Using the theory developed in the previous sections, we will now present the existence of bond currents in molecules under the zero net current condition. We will discuss different chemical compounds that show different loop current behavior.

In the literature on thermoelectric effects in single molecules, the Seebeck coefficient is calculated using eq. (4.5). As discussed in section 4.2.1, this equation correctly requires the condition $I = 0$, but influenced by the classical consideration it is further assumed that local currents vanish. With the described transfer matrix theory, we will show that non-zero bond currents exist in single molecule Seebeck measurement. This interesting effect is not described in the literature.

The bond currents are calculated in Mathematica using eq. (5.51). The equation takes the coefficients from the full wave function derived in section 5.2 as an input. The complete input is the molecule Hamiltonian, the coupling vectors $\mathbf{\Gamma}_\alpha$, reservoir temperatures, relative chemical potential $\mu_L - \varepsilon_0$ and the atom coordinates in the honeycomb lattice. We shall only look at fully conjugated hydrocarbons, and the hopping amplitude $t = 2.539$ eV is used between all carbon atom sites [33]. The temperatures are set to 290 K (25 meV) and 301.8 K (26 meV) for the left and right reservoir, respectively. Unless otherwise stated, the chemical potential of the left reservoir relative to the on-site energies is set to $\mu_L - \varepsilon_0 = 1$ eV , which is between the HOMO and LUMO energies in the discussed examples. The chemical potential of the right reservoir μ_R is calculated in each case, so that the total current cancels, $I = 0$. All bond currents presented in this section are represented as arrows pointing in the current flowing direction, and the current intensities are given in nA. Due to numeric noise, a cut-off $J_\mathrm{cutoff} = 0.1$ pA is used so that currents $J < J_\mathrm{cutoff}$ are set to zero.

The local currents are sensitive to the coupling between the molecule and contacts. This coupling strength varies depending on the contact material, the binding group in the molecule, etc. For simplicity we have chosen the coupling t, which also describes the coupling between carbon atom sites.

The resulting currents are therefore primarily assessed in a qualitative way. However, we want to get a rough estimate of the induced magnetic field strength in the center of a benzene ring. The current is assumed to flow in a perfect ring with radius $a = 1.39$ Å, which is the distance from the center to the carbon atoms. The Biot-Savart law reduces to $B_\mathrm{center} = \frac{\mu_0 I}{2a}$ and a loop current in a benzene ring can be converted into the magnetic field strength

$$I_\mathrm{loop} = 1 \text{ nA} \quad \rightarrow \quad B_\mathrm{center} = 4.5 \cdot 10^{-6} \text{ T} \,. \tag{5.55}$$

We did not yet study the effects of the magnetic fields induced by thermoelectric ring currents, but the above relation is included to give an idea about the field strength.

We will start by looking at benzene to build some intuition about the internal current effect. In 5.4.2 we will show how neighboring current loops with both the same and opposite directions can be generated in naphthalene depending on the lead connection sites. Similarly we find separated current loops of opposite directions in anthracene in section 5.4.3.

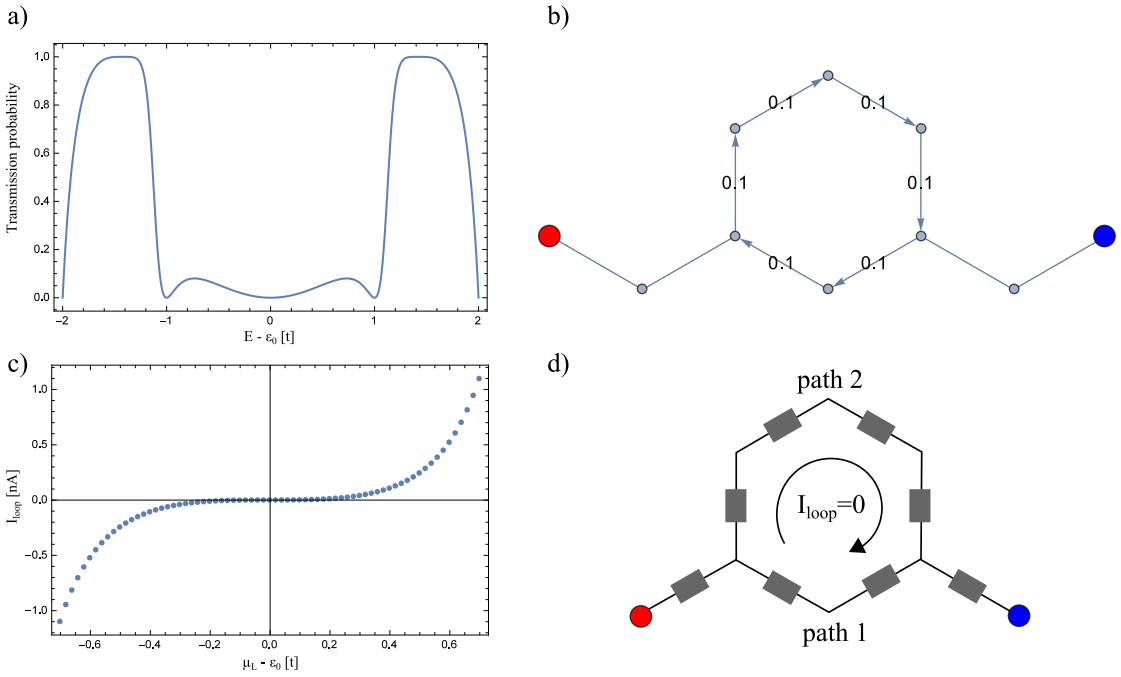

FIGURE 5.3: Calculations of meta-coupled benzene. a) The transmission probability through the molecule. b) The result from the bond current calculation, where the blue and red dots indicate the cold and hot leads. c) Loop currents for different $\mu_L - \varepsilon_0$. d) Naive circuit model that fails to explain the currents. The energies are in units of the hopping amplitude.

5.4.1 Benzene

In this section we will study bond currents in benzene. We will first present results of meta-coupled benzene and then see the effects of substitution in para-coupled benzene.

Meta-Coupled Benzene

As a first example, we consider meta connected benzene through which traveling electrons can take two chemically different paths. The total transmission probability through the molecule $\mathcal{T}(E) = |t(E)|^2$ calculated using eq. (5.31) is shown in fig. 5.3a. The shape of the function is influenced by the coupling between the molecule and the contacts. If the coupling is weakened, the function will become smoothed peaks around the orbital energies of the molecule. The highest occupied molecular orbital (HOMO) and lowest unoccupied molecular orbital (LUMO) have energies $-t$ and t respectively, which are obtained by solving the eigenvalue problem of the Hückel Hamiltonian. In the energy window between these orbital energies, we see that $< 10\%$ of the particles are being transmitted through the molecule.

The bond currents are shown in fig. 5.3b for $k_B\Delta T = 1$ meV and $\mu_L - \varepsilon_0 = 1eV$. As hypothesized, the result demonstrates the existence of internal currents even though there is no net current through the molecule. The current loop in the benzene ring has the intensity 0.1 nA. In order to examine how the current is affected by gating the molecule, the loop current is calculated for different relative energies $\mu_L - \varepsilon_0$ and plotted in fig. 5.3c. We see that the loop current disappears if the reservoir chemical potential

is equal to the on-site energy while the current intensity increases with the chemical potential in an uneven fashion. An intuitive explanation for the vanishing currents at $\mu_L = \varepsilon_0$ is that the current is carried partly by electrons and holes so that the "Seebeck coefficient" of each path is zero.

To model the effect, we naively start by considering the molecule as a circuit in which each bond is represented by a thermoelectric element with the electrical resistance R_{bond} and the Seebeck coefficient S_{bond}. This is shown schematically in fig. 5.3d. From the introductory section 1.3 on thermoelectric elements in a circuit, we know that a loop current in a parallel setup is $I_{\text{loop}} = \frac{S_2 - S_1}{R_1 + R_2}\Delta T$. The Seebeck coefficient for the serial connected bond components in path 1 reduce to $S_1 = \frac{S_{\text{b}} R_{\text{q,bond}} + S_{\text{bond}} R_{\text{q,bond}}}{R_{\text{q,bond}} + R_{\text{q,bond}}} = S_{\text{bond}}$ and consequently the two paths have the same Seebeck coefficient $S_1 = S_2 = S_{\text{bond}}$. This naive model therefore predicts $I_{\text{loop}} = 0$ no matter what conjugated hydrocarbon compound we choose and is not valid to describe the loop current effect.

If we instead think of each path as a single thermoelectric component which is sensitive to the chemical structure of the path, the two paths in meta benzene would have $S_1 \neq S_2$ and consequently $I_{\text{loop}} \neq 0$. By chemical structure we mean number of atom sites, side chains, etc. This consideration is supported by the results in the following subsection and it is used on the more complicated anthracene in section 5.4.3.

Substitution of Para-Coupled Benzene

In this subsection we will examine the effects of substitution in para-coupled benzene. We will find that compounds with two chemically identical paths have no internal current loops.

From meta coupled benzene, we learned that the internal current loop could not be described by the simple circuit model in fig. 5.3d. Instead we guessed that chemically different paths can be thought as thermoelectric components with different Seebeck coefficients. To investigate this further, we calculate the currents in both unsubstituted and doubly substituted para benzene as shown in fig. 5.4a and b. In both compounds the two paths are chemically identical and we see that there is no current loop.

For the mono-substituted vinylbenzene in fig. 5.4c, the side chain intuitively alters the electron density along the upper branch. Again we see the existence of a current loop due to the chemically different paths.

With these results we have build some intuition on internal current loops in single molecule Seebeck measurements. If the molecule has two paths that are chemically identical, no internal current loops exist. For chemically different paths, we calculated loop currents. We will now turn to more complicated compounds and see the existence of different loop configurations.

5.4.2 Naphthalene

In this section we will consider naphthalene, in which two neighboring current loops with either the same or opposite directions can be generated.

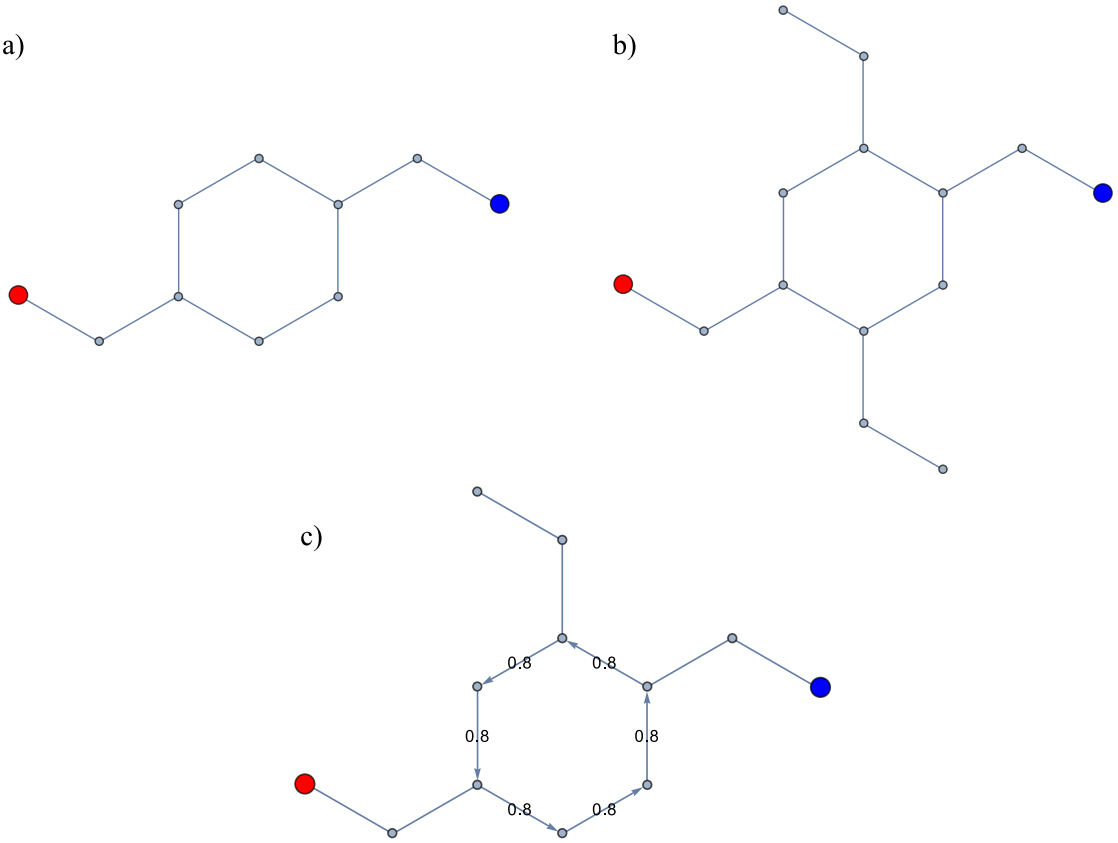

FIGURE 5.4: Results from the bond current calculation of para-connected benzene (a), divinylbenzene (b) and vinylbenzene (c). For a and b, the two paths are chemically identical and the internal currents are zero. The reverse argument holds for c.

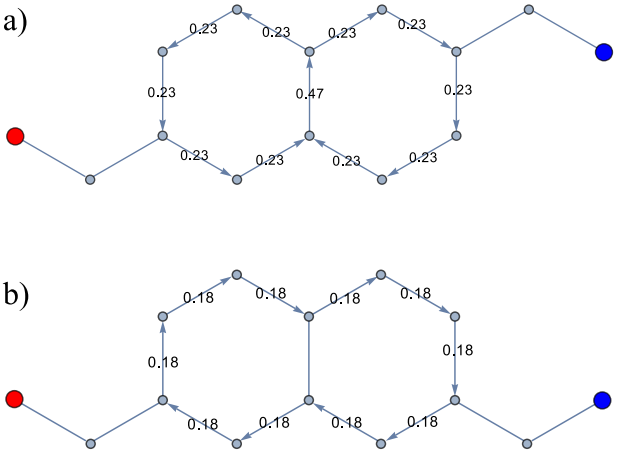

FIGURE 5.5: Bond current results for naphthalene coupled in two different ways. The generated ring currents have with opposite (a) and same (b) directions.

In the previous section we investigated different single ring compounds. We will now consider the double ring structured naphthalene. If the two leads are coupled to different rings, there are six combinations of attachment. The calculated bond currents for two interesting cases are shown in fig. 5.5. In 5.5a we see that the neighboring current loops have opposite directions. The similar result appears for the other possible setup in which the leads are attached in a 180 degree rotational symmetric fashion (see appendix A).

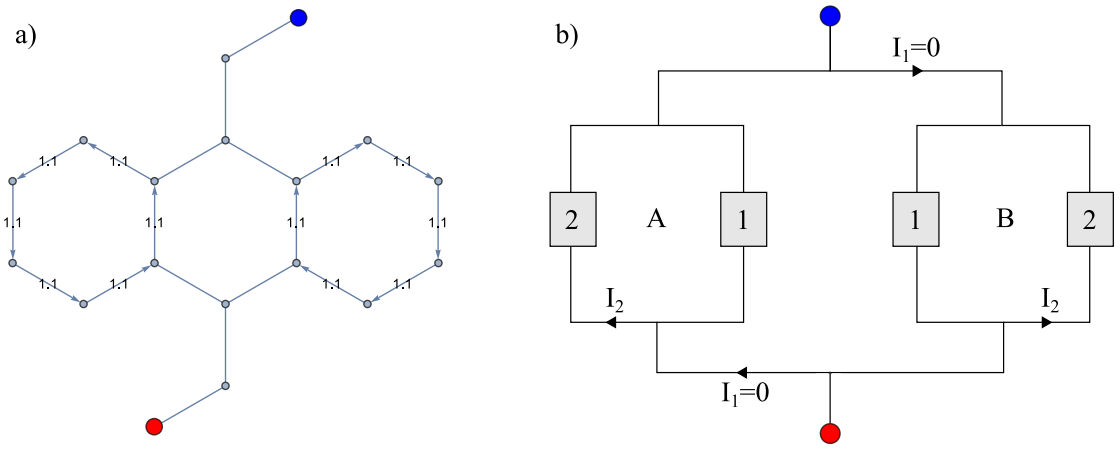

FIGURE 5.6: a) Result from bond current calculation on anthracene. b) A circuit model of the anthracene setup.

If naphthalene is connected in such a way that the setup is mirror symmetrical, current loops with the same direction appear as shown in fig. 5.5b. Since the currents are of the same intensity, the local current in the center bond cancels. Effectively a single current loop therefore forms in perimeter of the naphthalene. For more results on naphthalene, see appendix A.

These results are interesting from a theoretical perspective. Remember that the currents are generated without any net electric current flowing through the molecules. Another way to induce such aromatic ring currents is by applied magnetic fields. This is for example used in hydrogen nuclear magnetic resonance spectroscopy, where the currents alter the chemical environment around the hydrogen atoms, which can be detected in the chemical shifts. For naphthalene the magnetically induced ring currents have been calculated [34] to have the same form as the result in fig. 5.5b. The induction of the neighboring current loops of opposite directions in fig. 5.5b is therefore unique to the discussed thermoelectric experimental conditions. It is yet to be studied whether these discovered results have any possible applications.

5.4.3 Anthracene

In this section, we will see that separated current loops with opposite directions can be generated in anthracene.

Unsubstituted anthracene can theoretically be connected to leads in fifteen different ways. Consider first the case in which the leads are attached to the middle ring with the results shown in fig. 5.6a. We observe the existence of two current loops with different directions, but in contrast to the case of naphthalene, the two aromatic ring currents are separated in space. Again this is an interesting result from a theoretical perspective. We did not yet study the similarities between magnetically and thermally driven ring currents in depth, but intuitively this result of opposite directed and separated ring currents is unique to the thermoelectric induction.

The result can be understood by considering the different paths as thermoelectric components just as we did for benzene. Remember that chemically identical paths have the same Seebeck coefficient according to our model. For the particular case of anthracene,

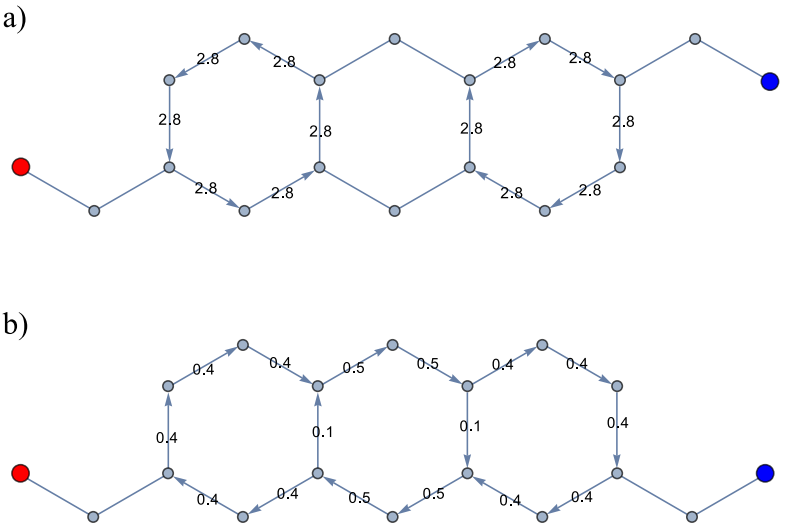

FIGURE 5.7: Results for unsubstituted anthracene connected in two different ways.

the circuit is sketched in fig. 5.6b. For the big loop, charge carriers can travel from the hot to cold reservoir through either A or B. But since these are chemically identical, the current in the big loop cancels:

$$I_1 = \frac{S_\mathrm{A} - S_\mathrm{B}}{R_\mathrm{A} + R_\mathrm{B}} \Delta T = 0 \tag{5.56}$$

Along A, path 1 and 2 are chemically different because the number of atom sites differ. There is therefore a non-zero loop current I_2:

$$I_2 = \frac{S_2 - S_1}{R_1 + R_2} \Delta T \neq 0 \tag{5.57}$$

Since B is the mirror of A, a loop current with the same intensity but opposite direction flows in B. With this circuit consideration, we have thus explained the results in fig. 5.6a.

We now want to study the anthracene analog to the naphthalene results in fig. 5.5. For napthtalene, we observed that leads connected in a 180 degree rotational symmetric manner gave rise to current loops of opposite directions. The results from anthracene follow the same logic, as shown in fig. 5.7a. Since the number of rings is uneven, the current cancels in the middle ring, while the outer ring currents are of opposite directions. When leads were connected to naphthalene in a mirror symmetrical way, loop currents with the same direction showed up. Again, the similar configuration appear in anthracene where all three ring currents have the same direction. The current intensities are almost the same in all rings, and the main part of the current therefore flows along the perimeter of the anthracene compound as shown in fig. 5.7b. More results of anthracene are shown in appendix A, where we for example see plus-plus-minus configurations of ring currents.

To predict the directions of the aromatic ring currents, more compounds and different energies $\mu_L - \varepsilon_0$ need to be analyzed. Our simple method of comparing two paths

only tells whether or not a current loop will exist. The link between the direction of the current loops and the attachment of electron donating/withdrawing side groups, HOMO/LUMO mediated transport, etc. is not yet found.

To sum up, we have described the theory to calculate local bond currents in any molecule. For a few aromatic systems, we presented thermoelectrically driven ring currents, and a simple method for predicting the existence of the currents was described. Among the results, we saw that two loop current with either the same or different directions could be generated depending on the coupling to the contacts. Any applications of these observations are yet to be studied.

Chapter 6

Conclusions and Outlook

In this thesis, we have discovered the existence of internal electric current loops in thermoelectric measurements under the zero net current conditions. The current loops were presented in macroscopic systems by solving boundary value problems with the linear transport equations, as well as in single molecules using Hückel theory and the transfer matrix formalism.

Initially, we examined the experimental results of a thickness dependent Seebeck measurement. The tip-setup was modeled by a serial circuit model including a calculated thermal constriction resistance, and the obtained characteristic b-value was a factor of 25 off compared to the experimental data. Supported by the literature, we argued that direct modeling is a challenging task due to the many unknowns. However, the characteristic line shape of the experimental data was reproduced, and we concluded that the measured length dependence was caused by the experimental setup.

In the process of calculating thermopower in the 3D inhomogeneous experimental setup, we discovered a general misassumption in the literature: It is assumed that the cancelation of the electric net current in a Seebeck measurement causes the electric current densities to vanish. We argued, why this assumption is wrong and used the model of parallel connected thermoelectric elements and the manipulated transport equation to show that currents densities will exist when $\nabla S \times \nabla T \neq 0$. We developed a FEM procedure to calculate both the temperature map, electrical potential field and current densities of any inhomogeneous setup. Top-gated graphene of a few μm was used as a realistic example and we estimated the magnetic field induced by the loop currents to have the strength of the order 10^{-8} T, which should be experimentally detectable.

Based on our discovery of internal currents in macroscopic inhomogeneous Seebeck measurements, we set up the hypothesis that such currents also exist in single molecule measurements. Using Hückel theory and the transfer matrix method, we developed the theory to obtain local bond currents in an arbitrary molecule, and the results confirmed our hypothesis. Several aromatic hydrocarbons were investigated and by analyzing the results, we found that the existence of ring currents can be predicted by the simple parallel circuit consideration: If two paths in the molecule are chemically different, an aromatic ring current exist, while the currents cancel, if the paths are chemically identical. For differently connected napthalene and anthracene molecules, we showed the

existence of two ring currents with different directions. These configurations of ring currents are unique to the thermoelectric experimental conditions in comparison to aromatic currents induced by applied magnetic fields.

6.1 Outlook

In this thesis, we demonstrated that internal currents exist in macroscopic inhomogeneous setups in which $\nabla S \times \nabla T \neq 0$. We showed that the developed FEM calculation procedure did not calculate significantly different Seebeck coefficients when compared to the parallel circuit model. However, it would be interesting to study whether the new calculation procedure affects other quantities such as the figure of merit.

In chapter 2 on the tip experiment, we assumed that the Seebeck coefficient of the BDT sample was independent on the layer thickness. This assumption was based on a comparison with the experimental results of length dependent Seebeck coefficients in single molecules in section 4.2.2. The systems are not directly comparable, however, and it would be interesting to model the Seebeck coefficient of the BDT sample by e.g. intermolecular hopping between the BDT compounds. Moreover, we need to take a deeper look into the calibration of the tip-setup in order to be able to measure Seebeck coefficients of unknown compounds.

For single molecules, we set up some intuition to predict when to expect the aromatic ring currents. Future research will be to study whether we can predict directions and intensities based on either the molecular structures or the HOMO/LUMO. Furthermore, it would be interesting to investigate whether the thermoelectrically induced ring currents can lead to any applications.

Appendix A

Aromatic Ring Currents

In this appendix we present bond current calculations of differently connected naphthalene and anthracene. These are included to provide the reader with a broad variety of calculations in contrast to the small selection in the thesis. The calculations are done at $\mu_L = \varepsilon_0 + 1eV$ with the temperatures 25 meV and 26 meV.

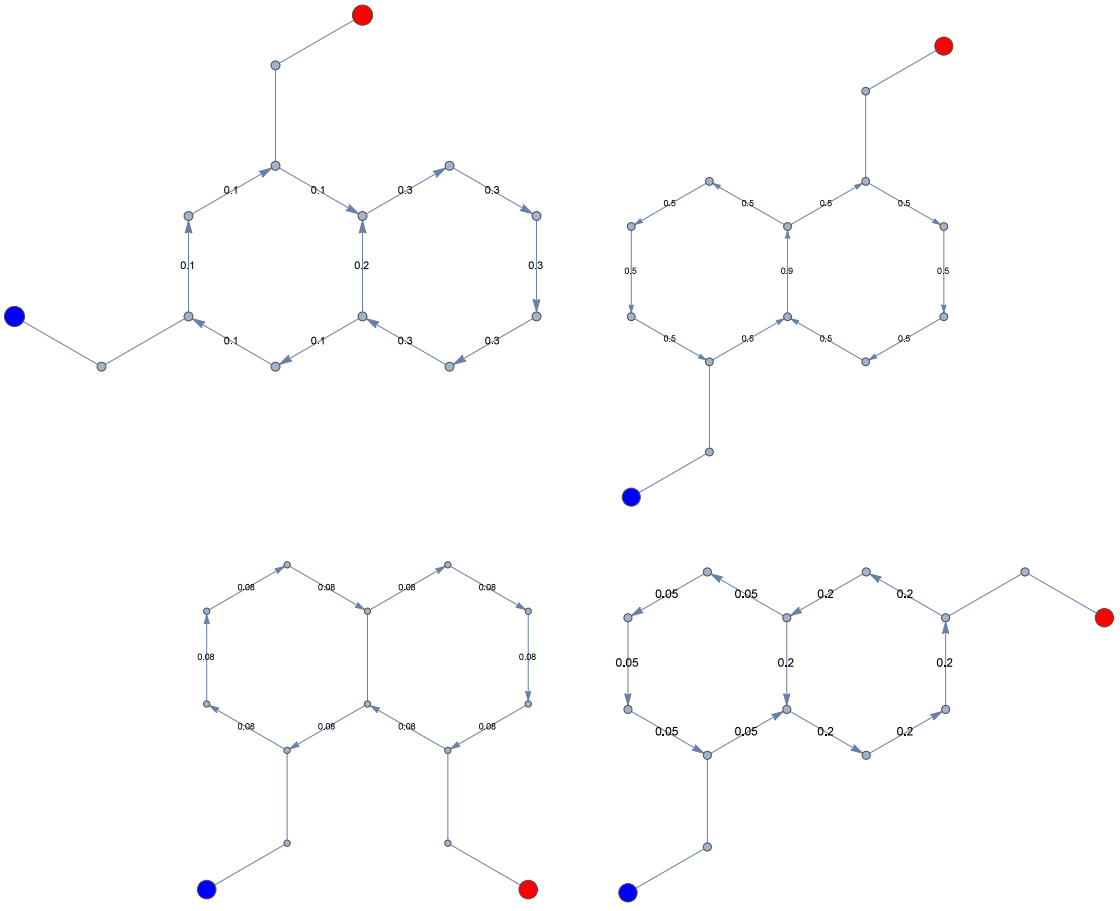

FIGURE A.1: Calculations of differently connected naphthalene.

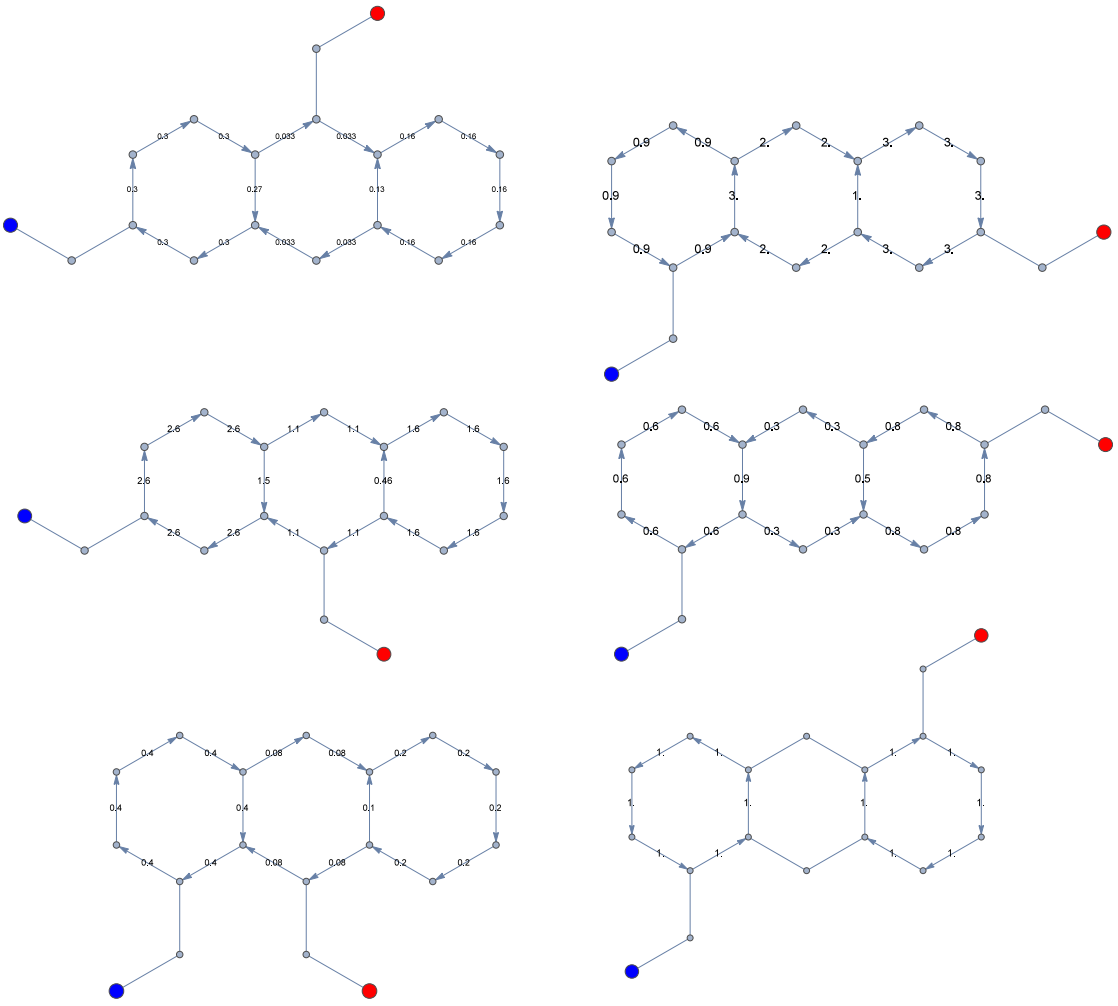

FIGURE A.2: Calculations of differently connected anthracene.

Bibliography

[1] Solyom, J. *Fundamentals of the Physics of Solids*; Springer, 2007.

[2] Callen, H. B. *Physical Review* **1948**, *73*, 1349–1358.

[3] Marder, M. P. *Condensed matter physics*; John Wiley & Sons, 2010; pp 483–504.

[4] Onsager, L. *Physical Review* **1931**, *37*, 405–426.

[5] Kaye & Laby Online, Tables of Physical & Chemical Constants. 1995; www.kayelaby.npl.co.uk.

[6] Lasance, C. J. M. The Seebeck Coefficient. 2006; http://www.electronics-cooling.com/2006/11/the-seebeck-coefficient/.

[7] Kim, N.; Domercq, B.; Yoo, S.; Christensen, A.; Kippelen, B.; Graham, S. *Applied Physics Letters* **2005**, *87*, 1–3.

[8] Vargas-almeida, A.; Olivares-robles, M. A.; Camacho-medina, P.; Nacional, I. P.; Esime-cul, S.; Ana, A. S. **2013**, 2162–2180.

[9] Pennelli, G. *Beilstein Journal of Nanotechnology* **2014**, *5*, 1268–1284.

[10] Zhao, L.-D.; Lo, S.-H.; Zhang, Y.; Sun, H.; Tan, G.; Uher, C.; Wolverton, C.; Dravid, V. P.; Kanatzidis, M. G. *Nature* **2014**, *508*, 373–7.

[11] Jackson, W. D. *Classical Electrodynamics*, 3rd ed.; John Wiley & Sons, 1999.

[12] Venkatasubramanian, R.; Siivola, E.; Colpitts, T.; O'Quinn, B. *Nature* **2001**, *413*, 597–602.

[13] Poler, C.; Edward, C. *Langmuir* **1995**, *11*, 2689–2695.

[14] Majumdar, a. *Annual Review of Material Science* **1999**, *29*, 505–585.

[15] Gomès, S.; Assy, A.; Chapuis, P.-O. *Physica Status Solidi (a)* **2015**, *212*, 477–494.

[16] Apertet, Y.; Ouerdane, H.; Goupil, C.; Lecoeur, P. *Physical Review B - Condensed Matter and Materials Physics* **2012**, *85*, 1–3.

[17] Fu, D.; Levander, a. X.; Zhang, R.; Ager, J. W.; Wu, J. *Physical Review B - Condensed Matter and Materials Physics* **2011**, *84*, 1–6.

[18] Anatychuk, L. I.; Prybyla, a. V. *Journal of Electronic Materials* **2011**, *40*, 1304–1310.

[19] Anatychuk, L. I.; Luste, O. J.; Kuz, R. V.; Strutinsky, M. N. *Journal of Electronic Materials* **2011**, *40*, 856–861.

[20] Ziolkowski, P.; Karpinski, G.; Dasgupta, T.; Müller, E. *Physica Status Solidi (A) Applications and Materials Science* **2013**, *210*, 89–105.

[21] Bian, Z.; Shakouri, A.; Shi, L.; Lyeo, H. K.; Shih, C. K. *Applied Physics Letters* **2005**, *87*, 2003–2006.

[22] Huang, C. C.; Hung, C. I. *International Journal of Thermal Sciences* **2013**, *64*, 121–128.

[23] Zuev, Y. M.; Chang, W.; Kim, P. *Physical Review Letters* **2009**, *102*, 1–4.

[24] Bergfield, J. P.; Ratner, M. a. *Physica Status Solidi (B) Basic Research* **2013**, *250*, 2249–2266.

[25] Xu, B.; Tao, N. J. *Science (New York, N.Y.)* **2003**, *301*, 1221–1223.

[26] Buttiker, M.; Imry, Y.; Landauer, R.; Pinhas, S. *Physical Review B* **1985**, *31*, 6207–6215.

[27] Dubi, Y.; Di Ventra, M. *Reviews of Modern Physics* **2011**, *83*, 131–155.

[28] Kim, D.; Yoo, P. S.; Kim, T. *Journal of the Korean Physical Society* **2015**, *66*, 602–606.

[29] Widawsky, J. R.; Chen, W.; Vázquez, H.; Kim, T.; Breslow, R.; Hybertsen, M. S.; Venkataraman, L. *Nano Letters* **2013**, *13*, 2889–2894.

[30] Reddy, P.; Jang, S.-Y.; Segalman, R. a.; Majumdar, A. *Science (New York, N.Y.)* **2007**, *315*, 1568–1571.

[31] Jido, Y.; Inagaki, T.; Fukutome, H. *Progress of Theoretical Physics* **1972**, *48*, 808–825.

[32] Bruus, H.; Flensberg, K. *Many-Body Quantum Theory in Condensed Matter Physics*; Oxford University Press, 2004.

[33] Bursill, R. J.; Castleton, C.; Barford, W. *Chemical Physics Letters* **1998**, *294*, 305–313.

[34] Steiner, E.; Fowler, P. W. *Journal of Physical Chemistry A* **2001**, *105*, 9553–9562.